The Astrophysical Journal, 1011:131 (20pp), 2026 November 1 https://doi.org/10.3847/1538-4357/aea61d
© 2026. The Author(s). Published by the American Astronomical Society.
OPEN ACCESS

MSA-3D: Uncovering Weak Active Galactic Nuclei and Resolved Outflows in Disguise in $z \sim 1$ Star-forming Galaxies

Namrata Roy[1,2], Alaina Henry[3], Tucker Jones[4], Ivana Barišić[4], Ryan L. Sanders[4,5], Kevin Bundy[6], Matthew A. Malkan[7], Themiya Nanayakkara[8], Karl Glazebrook[8], Timothy Heckman[9,1], Juan M. Espejo Salcedo[10], Xin Wang[11,12,13], Danail Obreschkow[14,15], and Tommaso Treu[16]

[1] School of Earth and Space Exploration, Arizona State University, Tempe, AZ 85287, USA; namratar@asu.edu
[2] Raman Research Institute, Sadashivanagar, C. V. Raman Ave., 560080, Bangalore, India
[3] Space Telescope Science Institute, 3700 San Martin Drive, Baltimore, MD 21218, USA
[4] Department of Physics and Astronomy, University of California, Davis, 1 Shields Avenue, Davis, CA 95616, USA
[5] Department of Physics and Astronomy, University of Kentucky, 505 Rose Street, Lexington, KY 40506, USA
[6] UCO/Lick Observatory, University of California, Santa Cruz, 1156 High Street, Santa Cruz, CA 95064, USA
[7] Department of Physics and Astronomy, University of California, 475 Portola Plaza, Los Angeles, CA 90095, USA
[8] Centre for Astrophysics and Supercomputing, Swinburne University of Technology, Hawthorn, VIC 3122, Australia
[9] The William H. Miller III Department of Physics and Astronomy, The Johns Hopkins University, Baltimore, MD 21218, USA
[10] Max-Planck-Institut für extraterrestische Physik (MPE), Giessenbachstraße 1., 85748 Garching, Germany
[11] School of Astronomy and Space Science, University of Chinese Academy of Sciences (UCAS), Beijing 100049, People's Republic of China
[12] National Astronomical Observatories, Chinese Academy of Sciences, Beijing 100101, People's Republic of China
[13] Institute for Frontiers in Astronomy and Astrophysics, Beijing Normal University, Beijing 102206, People's Republic of China
[14] International Centre for Radio Astronomy Research (ICRAR), M468, University of Western Australia, Perth, WA 6009, Australia
[15] Australian Research Council, ARC Centre of Excellence for All Sky Astrophysics in 3 Dimensions (ASTRO 3D), Australia
[16] Department of Physics and Astronomy, University of California, Los Angeles, CA 90095-1547, USA
Received 2025 October 14; revised 2026 August 25; accepted 2026 September 9; published 2026 October 29

Abstract

We present spatially resolved rest-optical spectroscopy of 38 star-forming galaxies at $0.5 < z < 1.5$ from the JWST/NIRSpec Micro-Shutter Assembly (MSA)-3D survey, which employs a slit-stepping strategy to build integral field unit–like data cubes with a spatial sampling of $\sim 0.''1$. We map emission-line morphology, excitation, and kinematics of the warm-ionized gas using [N II]/Hα, [S II]/Hα, and [O III]/Hβ. Relative to $z \sim 0$ galaxies at fixed stellar mass, our sources show systematically lower [N II]/Hα and [S II]/Hα and elevated [O III]/Hβ, consistent with harder radiation fields and lower metallicities. Radially, [O III]/Hβ profiles are typically flat or mildly positive, whereas [N II]/Hα also remains flat or declines outward, mirroring metallicity trends. On kiloparsec scales, we find a strong positive correlation between [N II]/Hα and velocity dispersion (σ), linking local excitation to turbulent or shock-driven kinematics. Six galaxies ($\sim$16% of the sample) host spatially localized regions with elevated [N II]/Hα, high EW(Hα), and $V_{\rm rms} \equiv \sqrt{V^2 + \sigma^2} > 250$ km s^{-1}, indicative of weak active galactic nucleus (AGN) activity, shocks, or outflows. For these candidates, we infer modest warm-ionized outflow rates of $1-4\,M_\odot\,{\rm yr}^{-1}$ and kinetic powers $\sim$0.1%−1% of the AGN bolometric luminosity (from central [O III] or Hα). These values place our sample at the low-energy tail of known AGN-driven outflows yet in continuity with $\dot{M}_{\rm out}$–$L_{\rm AGN}$ scaling relations across $0 < z < 6$. A completeness assessment shows MSA-3D is sensitive to AGN with $L_{\rm AGN} \gtrsim 10^{43}$ erg s^{-1}, underscoring both the promise and current limitations of detecting weak AGN activity in distant galaxies with resolved spectroscopy.

Unified Astronomy Thesaurus concepts: Active galaxies (17)

1. Introduction

Rest-frame optical nebular emission lines provide a powerful window into the physical conditions of the interstellar medium (ISM) in star-forming galaxies. The collisionally excited and recombination lines powered by young stars, active galactic nuclei (AGN), or shocks trace the density, temperature, chemical, and ionization state of the ISM, and offer critical insights into star formation (SF) and feedback processes. The relative strengths of key emission lines, particularly when plotted as diagnostic line ratios, allow us to disentangle the dominant ionizing sources in galaxies and characterize their internal conditions. One of the most widely used diagnostic tools is the Baldwin–Phillips–Terlevich (BPT) diagram (J. A. Baldwin et al. 1981), which uses [O III] λ5007/Hβ versus [N II] λ6584/Hα (or [S II] λ6717,31/Hα) line ratios to distinguish between ionization from SF, AGN activity, and low-ionization nuclear emission-line regions (LINERs). In the local Universe, galaxies trace a well-defined star-forming sequence in this diagram. Decreasing [O III]/Hβ and increasing [N II]/Hα reflect a progression of increasing metallicity and decreasing ionization parameter (L. J. Kewley et al. 2019), with AGN and LINERs occupying a distinct, separate region (L. J. Kewley et al. 2001; G. Kauffmann et al. 2003). For sources lacking complete sets of lines, alternative diagnostics such as the [N II]/Hα versus EW(Hα) diagram, known as the WHAN diagnostic (R. Cid Fernandes et al. 2011), are used to distinguish between SF and AGN excitation sources.

Over the past decade prior to JWST, ground-based near-infrared spectrographs and Hubble Space Telescope (HST)/

Original content from this work may be used under the terms of the Creative Commons Attribution 4.0 licence. Any further distribution of this work must maintain attribution to the author(s) and the title of the work, journal citation and DOI.

WFC3 grism spectroscopy enabled optical emission-line studies of galaxies at $z \sim 1$–3 (C. C. Steidel et al. 2014; A. L. Coil et al. 2015; A. E. Shapley et al. 2015; I. G. Momcheva et al. 2016; R. L. Sanders et al. 2016; A. Henry et al. 2021). These surveys revealed that high-redshift galaxies exhibit systematically lower metallicities, higher star formation rates (SFRs), harder ionizations, and elevated gas velocity dispersions compared to local systems and fixed stellar mass (I. Shivaei et al. 2015; N. M. Förster Schreiber et al. 2019; E. Wisnioski et al. 2019). Additionally, star-forming galaxies at $z > 1$ consistently show offsets in the BPT diagram relative to their low-redshift counterparts, often with elevated [O III]/Hβ at fixed [N II]/Hα. This suggests contributions from one or more factors: harder ionizing spectra, evolving ISM conditions, and enhanced nitrogen enrichment at higher redshift (C. C. Steidel et al. 2014; A. E. Shapley et al. 2015; D. Masters et al. 2016; R. L. Sanders et al. 2016; A. E. Shapley et al. 2019; R. L. Sanders et al. 2023).

With the launch of JWST, we have entered a new era of rest-optical diagnostics at high redshift. Thanks to the sensitivity and spectral coverage of JWST/NIRSpec and MIRI, rest-frame optical lines can now be studied out to $z \sim 9.5$. Early results from programs such as AURORA (R. L. Sanders et al. 2026; A. E. Shapley et al. 2025; M. W. Topping et al. 2025), CEERS (R. L. Sanders et al. 2023; A. E. Shapley et al. 2023; B. E. Backhaus et al. 2024), GLASS (J. R. Trump et al. 2023), JADES (A. J. Cameron et al. 2023), and other campaigns (K. Nakajima et al. 2023; M. Curti et al. 2023) confirmed continued offsets of high-redshift galaxies ($z \sim 1-7$) in BPT space compared to the local sequence, and revealed a wide diversity in ionization conditions and metallicities, even among galaxies on the star-forming main sequence (SFMS).

While these recent spectroscopic efforts have significantly advanced our understanding of the redshift evolution of ISM properties including excitation, ionization, and chemical abundances through integrated emission-line diagnostics, accompanying spatially resolved spectroscopy is needed to probe the internal structure of galaxies. Integral field unit (IFU) spectroscopy is essential to dissect the local interplay between SF, chemical enrichment, gas flows, and feedback and to capture how nebular emission-line properties vary across different physical regions within individual galaxies at higher redshift. This has been demonstrated extensively at low redshift by several large IFU surveys such as MaNGA (K. Bundy et al. 2015), CALIFA (S. F. Sánchez et al. 2016), and PHANGS-MUSE (E. Emsellem et al. 2022) and at intermediate redshift by SINS using SINFONI IFU ($z \sim 1-2$; R. Genzel et al. 2011; K. Glazebrook 2013; N. M. Förster Schreiber et al. 2019). Those studies have revealed that galaxies often host spatially complex ionization structures, with the same galaxy simultaneously exhibiting AGN-like, LINER-like, and star-forming excitation in different regions depending on local conditions (M. Sarzi et al. 2010; F. Belfiore et al. 2016). Resolved emission-line maps are thus crucial to trace radial metallicity gradients, distinguish ionization mechanisms between galaxy centers and outskirts, and detect weak AGN-driven outflow or shock signatures that may be unidentifiable in integrated global spectra.

Spatially resolved spectroscopy has been the key in uncovering weak outflow or inflow signatures that are often missed in integrated light due to their low surface brightness or small velocity offsets (N. Roy et al. 2018, 2021a, 2021b; G. Venturi et al. 2021; R. A. Riffel et al. 2024). A striking example of this is MaNGA's discovery of "red geyser" galaxies where large-scale biconical ionized-gas outflows driven by weak AGNs and neutral gas inflows were only detected through spatial mapping of kinematics and ionization and remained hidden in Sloan Digital Sky Survey (SDSS) single-fiber spectra (E. Cheung et al. 2016; N. Roy et al. 2021a, 2021b, 2021c). This is now particularly timely in the context of the high-redshift regime. Spatially resolved rest-frame optical spectroscopy at $z \sim 1$–3 has already been pioneered from the ground with IFU surveys such as SINS/zC-SINF and KMOS^{3D}, which established that high-redshift star-forming galaxies commonly show complex morphologies, resolved kinematic structure, metallicity gradients, and, in some cases, signatures of outflows and AGN-related excitation (R. Genzel et al. 2011; J. A. Newman et al. 2013; N. M. Förster Schreiber et al. 2014, 2019; G. Cresci et al. 2015; E. Wisnioski et al. 2015). More recently, JWST/NIRSpec IFU observations have extended such studies to higher redshift and revealed broad-line and heavily obscured AGN populations (Y. Harikane et al. 2023; I. Labbé et al. 2023; V. Kokorev et al. 2024; R. Maiolino et al. 2024; J. Matthee et al. 2024; H. Übler et al. 2024; D. D. Kocevski et al. 2025). While these studies have demonstrated the power of resolved spectroscopy at high redshift, the incidence of weak or subdominant AGN activity in otherwise normal star-forming galaxies remains poorly constrained, particularly at $z \sim 1$, where such signatures are easily diluted in integrated spectra and require spatially resolved diagnostics to isolate them.

In this paper, we present results from the `MSA-3D` program, which is a JWST/NIRSpec campaign using the slit-stepping mode of the Micro-Shutter Assembly (MSA) to acquire IFU-like spectroscopy. Using extremely efficient multiplexed observations with MSA slitlets, this program provides high-quality spatially resolved spectra for a large sample of 43 galaxies at $0.5 < z < 1.5$ simultaneously, in <10% of the time needed for an equivalent survey in the NIRSpec IFU mode (see I. Barišić et al. 2025; M. Ju et al. 2025, for more details on the MSA-3D program). This offers the opportunity to spatially resolve the ionized ISM in a relatively large sample of typical star-forming galaxies at $z \sim 1$, reaching subkiloparsec scales during the peak epoch of cosmic SF. Using high-resolution NIRSpec/MSA observations, we construct 2D maps of key emission lines, mainly Hα, Hβ, [N II], [S II], and [O III] across each galaxy, which enables a detailed investigation of internal gas morphology, ionization structure, and kinematics. We find a range of ionized-gas morphologies — from smooth disks to patchy, clumpy distributions, and, in some cases, spatial offsets between stellar-continuum and ionized-gas-resolved maps. Such morphologies are consistent with those seen in clumpy, gas-rich galaxies at $z > 1$ (B. G. Elmegreen 2007; R. Genzel et al. 2011), likely driven by disk instabilities, mergers, or local feedback.

Using slit-stepped NIRSpec cubes, we construct spatially resolved ionization diagnostic maps (BPT/WHAN) and construct averaged radial profiles of the principal nebular ratios—for, e.g., [N II]/Hα, [O III]/Hβ, and [S II]/Hα, to trace chemical enrichment, ionization structure, and the physical state of the ionized ISM across each galaxy. We place these spatial trends in context by comparing their overall character with representative results from $z \sim 0$ IFU surveys. This lets us

track how gas excitation conditions vary in galaxies across redshifts without relying on one-to-one calibrations.

We further examine the link between local ionization conditions and ionized-gas kinematics by comparing spaxel-scale line ratios with the line-of-sight velocity and velocity dispersion (σ). We show that a spatially resolved correlation exists between the [N II]/Hα ratio and σ locally across subgalactic regions in the entire sample, similar to trends noted in nearby systems (J. J. D'Agostino et al. 2019). By this analysis, we also identify a small subset of systems that exhibit compact, high-excitation zones and elevated dispersions. On closer inspection, the spectra from these regions are inconsistent with pure SF and, in a subset of cases, also show multiple kinematic components suggestive of mixed contributions from AGN photoionization, shocks, and outflow-heated gas, coincident with enhanced turbulence. These spatially resolved diagnostics reveal weak AGN/outflow activity that would be difficult to recognize in integrated spectroscopy. We measure associated mass-outflow rates and kinetic energies, and derive the lowest-energy tail of AGN feedback signatures accessible with JWST via this slit-stepping experiment. This underscores the instrument's power to expose small-scale feedback signatures and the internal dynamical complexity of $z > 1$ galaxies.

This paper is organized as follows: Section 2 describes the NIRSpec MSA-3D observations, sample selection, and emission-line fitting procedures. Section 3 presents the main results, focusing on spatially resolved emission-line maps, BPT diagnostics, and gas kinematics. In Section 4, we discuss the implications of the results, and we summarize our conclusions in Section 5.

2. Data

2.1. Observations and Sample Selection

This work is based on JWST NIRSpec spectroscopic observations from the Cycle 1 program GO 2136 (PI: T. Jones), which uses the NIRSpec MSA in slit-stepping mode to obtain spatially resolved spectroscopy of the sources. This approach enables the construction of pseudo-IFU data cubes, allowing us to spatially map rest-frame optical emission lines and continuum across galaxy disks at kiloparsec scales. A detailed description of the slit-stepping strategy and the 3D data cube reconstruction pipeline is provided in I. Barišić et al. (2025). The observations were taken using the G140H/F100LP grating and filter combination, providing high spectral resolution ($R \sim 2700$) across a wavelength range of $0.97\,\mu\mathrm{m} < \lambda < 1.82\,\mu\mathrm{m}$. This setup allows us to detect all the strong rest-optical nebular lines, primarily Hα, [N II]6584, [S II]6717, 6731, [O III]5007, and Hβ, within a single grating for galaxies within $0.5 < z < 1.7$. The reconstructed data cubes have a point-spread function (PSF) that is approximated by a 2D Gaussian with FWHM $= 0.''1 \times 0.''2$. These are sampled onto a spatial grid of $0.''08 \times 0.''08$, which corresponds to a spaxel size of 0.5−0.7 kpc for the redshift range $0.5 < z < 1.7$. The JWST data presented in this article were obtained from the Mikulski Archive for Space Telescopes (MAST) at the Space Telescope Science Institute. The specific observations analyzed can be accessed via doi:10.17909/8hkf-4e47.

The parent sample consists of 43 star-forming galaxies at $0.5 < z < 1.7$, selected to ensure that multiple strong rest-optical lines fall within the observed wavelength window. The galaxies are located in the Extended Groth Strip (EGS)—a well-studied field with extensive multiwavelength coverage. All targets benefit from existing photometric and spectroscopic data from HST, JWST, and Keck, due to their inclusion in major legacy surveys such as CANDELS (A. M. Koekemoer et al. 2011), 3D-HST (I. G. Momcheva et al. 2016), MOSDEF (M. Kriek et al. 2015), DEEP2 (J. A. Newman et al. 2013), and CEERS (S. L. Finkelstein et al. 2024). To ensure robust emission-line measurements across each galaxy, we visually inspected all data cubes and excluded five targets with inadequate signal-to-noise (S/N), specifically systems for which the brightest line (Hα or [O III] λ5007) had S/N < 2 in more than 90% of spaxels. This results in a final sample of 38 galaxies, which forms the basis for all analyses in this work.

Figure 1 illustrates the properties of the galaxy sample used in this work. We adopt stellar mass and SFR estimates from the 3D-HST catalog (I. G. Momcheva et al. 2016), and use ancillary high-resolution imaging from JWST/NIRCam (CEERS) and HST/Advanced Camera for Surveys+WFC3 (CANDELS) to contextualize the spatial distribution of line emission. We compute projected and deprojected galactocentric radii for each spaxel using structural parameters like position angle and axis ratio (b/a) derived from published catalogs based on GALFIT analyses of HST imaging (A. van der Wel et al. 2014).

2.2. Measuring Emission-line Ratios and Gradients

In this work, we analyze the spatially resolved ionization and kinematic properties of 38 star-forming galaxies at redshifts $0.5 < z < 1.7$, using JWST/NIRSpec MSA-3D spectroscopy. Our analysis focuses on extracting emission-line fluxes, velocity fields, and velocity dispersion maps from the data cubes to construct physical diagnostics across each galaxy.

We model the strongest rest-frame optical emission lines, primarily [O III]4959, 5007, Hβ, Hα, [N II]6548, 6584, and [S II]6717, 6731, by fitting Gaussian profiles with a single kinematic component on a spaxel-by-spaxel basis. For each galaxy, we fit Hα, [N II], and [S II] lines simultaneously using five separate Gaussians plus a linear continuum. To reduce degeneracies in low S/N regions, we tie the central velocity (v) and velocity dispersion (σ) of all lines in every spaxel, and fix the flux ratio of the [N II]λ6584/6548 doublet to the theoretical value of 2.94. For galaxies where [S II] is not detected or redshifted out of the spectral range, we use a simplified three-component model for Hα + [N II] alone. A similar approach is adopted for the [O III]λ4959,5007 and Hβ complex, where we fit a three-component model with a shared v and σ across lines, and fix the [O III]λ5007/4959 flux ratio to 2.98. All fits are performed independently in each spaxel. For spaxels used in the resolved BPT analysis, we require an S/N of S/N > 3 in all four primary emission lines, Hα, Hβ, [N II] λ6584, and [O III] λ5007. Spaxels failing this threshold are excluded from the BPT-based maps and classifications. For the WHAN analysis, we retain spaxels with reliable Hα and [N II] measurements and measurable EW(Hα), even when Hβ or [O III] are not detected with sufficient significance.

To characterize the ionization conditions across galaxies, we employ two commonly used diagnostics: the BPT diagram (J. A. Baldwin et al. 1981; L. J. Kewley et al. 2001; G. Kauffmann et al. 2003) and the WHAN diagram (R. Cid Fernandes et al. 2011). Where all four key lines—[O III], Hβ,

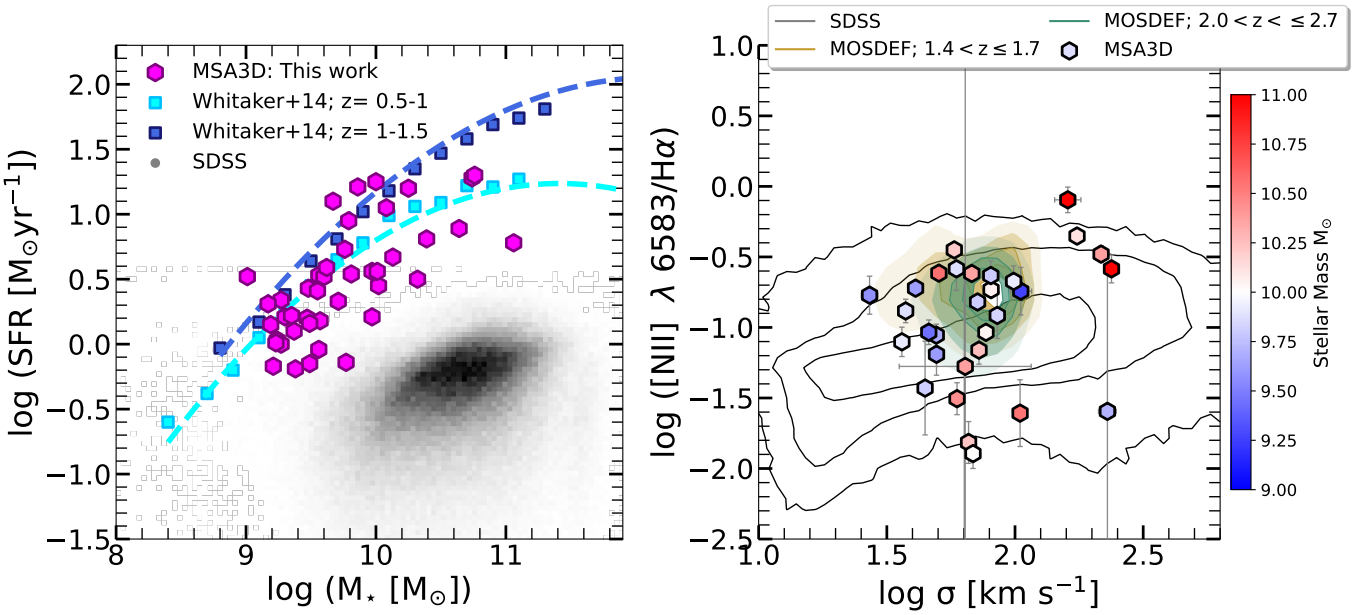


Figure 1. [Left] The star formation rate (SFR) versus stellar mass ($M_\star$) for MSA-3D galaxies (magenta hexagons), derived via multiwavelength SED fitting (A. M. Koekemoer et al. 2011; M. Stefanon et al. 2017). For comparison, we show the star-forming main-sequence (SFMS) relations at $0.5 < z < 1$ (cyan) and $1 < z < 1.5$ (blue) from K. E. Whitaker et al. (2014), along with the $z \sim 0$ SDSS galaxy population as a gray 2D histogram. Our sample shows closer agreement with the $0.5 < z < 1.0$ SFMS relation with a mean offset of ~0.27 dex. [Right] Emission-line excitation, traced by log([N II] λ6584/Hα), (the horizontal axis of the WHAN diagram) versus gas velocity dispersion (σ), for MSA-3D galaxies. Both quantities are measured from integrated spectra coadded within $2R_e$ apertures. Only systems with [N II] and Hα detected within the observed spectral window are shown (colored hexagons). They are color coded by stellar mass. Overplotted for reference are contours for SDSS galaxies at $z \approx 0$ (black) and MOSDEF galaxies at $1.4 < z < 1.7$ (yellow) and $2.0 < z < 2.7$ (green). They show almost no correlation in their integrated measurements.

Hα, and [N II]—are available, we use the [N II]/Hα versus [O III]/Hβ BPT diagram to distinguish between H II-region-like emission, composite excitation, LINER, and AGN-dominated regions. In cases where Hβ or [O III] does not fall in our observed wavelength range, we instead use the WHAN diagram, which combines [N II]/Hα with the equivalent width of Hα to classify ionization sources. We note that the WHAN diagnostic was originally calibrated in the local Universe (R. Cid Fernandes et al. 2011). Hence, its EW(Hα)-based boundaries may not map directly onto galaxies at $z \sim 1$ as main-sequence systems typically have higher specific SFRs and correspondingly larger Hα equivalent widths than local SDSS galaxies (E. Mármol-Queraltó et al. 2016). We therefore use the WHAN diagram as an empirical, resolved ionization diagnostic and do not use it as an individual, definitive AGN classifier. Elevated EW(Hα) alone is not interpreted as evidence for AGN activity. We identify candidate AGN/outflows regions only when the WHAN or BPT line ratio suggests nonstellar or mixed excitation, and they are spatially coherent and accompanied by disturbed ionized-gas kinematics, offsets from disk morphology, misalignment between gas and stellar-kinematic axis, and the presence of asymmetric, multicomponent line profiles.

Most galaxies in our sample do not show strong evidence for highly asymmetric wings or clear multicomponent structure in their emission-line profiles. We therefore adopt a single-component Gaussian fit to the emission-line profiles for all galaxies in the main analysis. The observed velocity dispersion ($\sigma_{\rm obs}$) from each Gaussian fit is corrected for instrumental broadening by subtracting the spectral resolution of the NIRSpec G140H grating in quadrature. We adopt a line spread function with FWHM ~5.2 Å, which corresponds to a varying spectral resolution $R \sim 1900-3500$ across the observed wavelength range. However, we note that the true NIRSpec resolution may be slightly higher than this approximation (A. J. Shajib et al. 2025), resulting in a mild overestimation of our intrinsic velocity dispersion (σ) values, especially near the instrumental resolution. We use the resulting σ and $V_{\rm rms}$ maps as empirical tracers of locally disturbed ionized gas across each galaxy. For the small subset of galaxies that do show evidence for multicomponent structure, we allow the model the flexibility to include either one or two Gaussian components, depending on which provides the better description of the data, and use that to identify evidence of outflows. Overall, however, the analysis presented in this work is based on the homogeneous single-component measurements.

To quantify radial gradients in emission-line ratios and velocity dispersion, we calculate the deprojected galactocentric distance of each spaxel from the galaxy center. Galaxy centers are defined as the peak of the continuum light, computed by collapsing the data cube along wavelength while masking strong emission lines. We adopt galaxy position angles and axis ratios (b/a) from available HST-based catalogs (A. van der Wel et al. 2014), allowing us to deproject each spaxel's radial distance and construct radial profiles for individual line ratios and kinematic properties. Radial distances are then normalized by the galaxy's effective radius (R/R_e) to compute radial gradients for each galaxy.

3. Results

3.1. Global Properties

We begin by characterizing the global properties of the MSA-3D sample. Understanding where these galaxies lie in relation to the SFMS is important, as both gas-phase

metallicity and ionization conditions are known to correlate with stellar mass and SFR (F. Mannucci et al. 2010; R. L. Sanders et al. 2016, 2021). Figure 1 (left panel) shows the distribution of our targets in the SFR–stellar mass plane. Stellar masses and SFRs are taken from multiwavelength spectral energy distribution (SED) fitting to the available HST photometry from the CANDELS survey, as reported in publicly released catalogs (A. M. Koekemoer et al. 2011; M. Stefanon et al. 2017). We adopt SFRs derived from SED fitting to ensure consistency across the sample, as the Hα and Hβ emission lines—which are commonly used for dust-corrected line-based SFR estimates—are not often simultaneously observed within the wavelength coverage (0.97 $-1.82\,\mu$m) of the G140H/F100LP grating used in the MSA-3D observations.

The MSA-3D galaxies (magenta hexagons), spanning $0.5 < z < 1.7$, exhibit stellar masses of $\log_{10}(M_\star/M_\odot) = 9 - 11$ and lie predominantly along the SFMS at $z \sim 1$. For reference, we include the parameterized main-sequence relations from Whitaker et al. (2014) at $z = 0.5-1.0$ (cyan-dashed line) and $z = 1.0-1.5$ (blue-dashed line), along with the local SDSS relation (gray-scale 2D histogram). Our sample shows closer agreement with the $0.5 < z < 1.0$ SFMS relation with a mean offset of ∼0.27 dex. In comparison, the average deviation of the MSA-3D SFRs from the $1.0 < z < 1.5$ relation of K. E. Whitaker et al. (2014) is larger at ∼0.5 dex, but still overall consistent except maybe a handful of sources where the offset goes to 1 dex. Our galaxies are thus representative of the typical star-forming population at $z \sim 1$, and are not extreme outliers in terms of SF activity.

In the right panel of Figure 1, we examine the dependence of gas-phase excitation, traced by [N II]λ6584/Hα (the x-axis of the traditional WHAN diagram) on the integrated gas kinematics (velocity dispersion, σ) within 2 R_e. Effective radii R_e are measured with GALFIT on the available HST/F160W imaging, and verified to be consistent with the M. Stefanon et al. (2017) catalog. For each source, we coadd all spaxels within $2R_e$ and fit the integrated spectrum with a Gaussian emission-line model plus a first-degree polynomial continuum. Line centers and dispersions are tied across the primary lines (Hα, [N II]$\lambda\lambda$6548,84, [S II]$\lambda\lambda$6717, 32, [O III]), following the per-spaxel fitting procedure described in Section 2. The resulting [N II]/Hα and velocity dispersion (σ) for all MSA-3D sources are shown as hexagons, colored by their stellar mass. The error bars indicate 1σ uncertainties (16th–84th percentile ranges) in the reported values.

Across the MSA-3D sample, we find no significant correlation between the [N II]/Hα and σ Pearson coefficient test: $r = 0.27$, $p = 0.25$. For context, we overlay MOSDEF galaxies at $z \sim 1.5$ and $z \sim 2.5$ (yellow- and green-filled contours) and the SDSS locus (black contours), which likewise show weak or absent trends. Coloring the MSA-3D points by stellar mass indicates that higher [N II]/Hα preferentially occurs at higher $M_\star$. This apparent positive trend is consistent with the mass–metallicity relation, given that [N II]/Hα correlates with gas-phase metallicity, and mass and metallicity are correlated (M. Pettini & B. E. J. Pagel 2004). A secondary dependence of [N II]/Hα on outflow-driven broadening in more massive systems may also contribute, resulting in enhanced σ in a few sources, which we explore further in later sections. Overall, MSA-3D galaxies occupy the parameter space expected for main-sequence star-forming galaxies at $z \sim 1$, while extending to lower stellar masses than most previous spatially resolved surveys at similar redshifts.

3.2. Integrated and Resolved BPT and WHAN Diagrams at z ∼ 1

Building on the global properties discussed above, we now investigate the dominant ionization mechanisms within our sample using both integrated and spatially resolved emission-line diagnostics. Specifically, we employ the classic [N II]/Hα versus [O III]/Hβ BPT diagram (J. A. Baldwin et al. 1981; S. Veilleux & D. E. Osterbrock 1987). Large spectroscopic surveys have shown that emission-line galaxies trace two distinct branches in the BPT diagram: a sequence at $\log([\text{N II}]/\text{H}\alpha) < -0.3$ associated with star-forming H II regions well reproduced by photoionization models of OB stars and the branch at higher [N II]/Hα linked to hard ionization sources like AGNs and Seyferts along with contribution from shocks and evolved stars from LINERs/LIERs (L. J. Kewley et al. 2001; G. Kauffmann et al. 2003; G. Stasińska et al. 2006; F. Belfiore et al. 2016). Thus, the BPT diagram using galaxy-integrated spectra demonstrates the dominant ionization mechanism responsible for ionizing the major portion of the ISM gas.

Figure 2 (left) presents the integrated BPT diagram for the subsample of galaxies with coverage in [O III], Hβ, Hα, and [N II] (magenta hexagons). Here, line fluxes are summed within 2 times the effective radii (R_e). For comparison, we overlay contours from SDSS ($z \sim 0$), and include high-redshift star-forming samples from AURORA ($z \sim 1-7$; A. E. Shapley et al. 2025), CEERS ($z \sim 2-6$; R. L. Sanders et al. 2023), and SINS/zC-SINF ($z \sim 1.5-2.5$; N. M. Förster Schreiber et al. 2019a). Theoretical and empirical demarcation lines from L. J. Kewley et al. (2001) and G. Kauffmann et al. (2003) are shown in blue and dashed black, respectively. Our galaxies fall below the L. J. Kewley et al. (2001) and G. Kauffmann et al. (2003) curves, unlike some of the higher-redshift sources from the AURORA survey, but display a broad range of [O III]/Hβ and [N II]/Hα ratios consistent with photoionization from young stars. Over 85% of the sample with simultaneous coverage of all four emission lines shows $\log([\text{O III}]/\text{H}\beta) > 0.3$ and $\log([\text{N II}]/\text{H}\alpha) < -0.8$ in their integrated line ratios. This clear preference to lie in the upper left region in the BPT locus is in agreement with previous results at $z > 1$ (A. E. Shapley et al. 2015; R. L. Sanders et al. 2016; A. L. Strom et al. 2017; M. Curti et al. 2023), and reflects moderately low metallicities at higher redshift. Galaxies at $z > 1$, on average, have harder ionizing spectra, higher ionization parameters, and lower metallicity (corresponding to lower N/O abundance ratios) at fixed stellar mass compared to $z \sim 0$ galaxies from SDSS. Our targets are representative of the $z \sim 1$ star-forming population in terms of excitation properties.

In order to include cases where [O III] and/or Hβ fall in the NIRSpec chip gap, remain undetected, or lie outside the G140H/100LP spectral coverage, we complement the BPT analysis with the WHAN diagram (R. Cid Fernandes et al. 2011), which only requires [N II] and Hα emission lines and is widely used to classify sources based on ionization source and stellar population age. The integrated WHAN diagram (Figure 2) is shown on the right panel, and has been derived for a larger subset (∼81%) of our sample due to the strategic choice of the G140H/100LP grating that includes Hα + [N II].

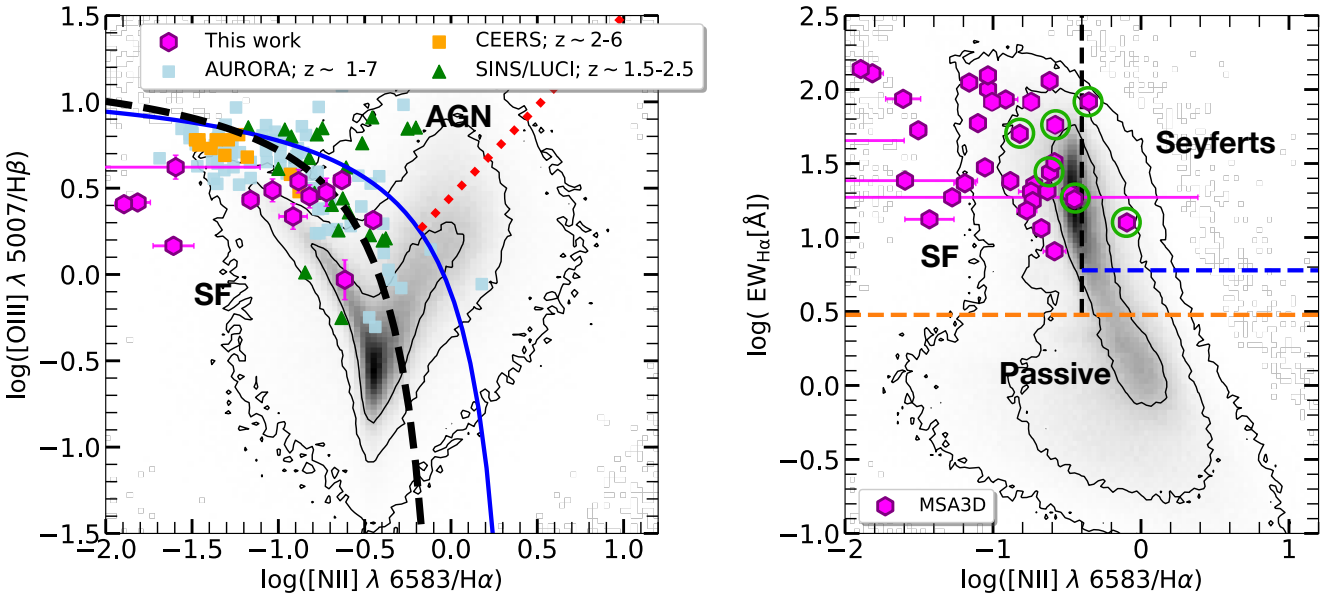


Figure 2. [Left] The integrated BPT diagram for MSA-3D galaxies (magenta hexagons), where emission-line fluxes are summed within $2R_e$. 13 out of the 38 galaxies in our sample have wavelength coverage of all four emission lines required for this diagram. For comparison, we overlay contours from SDSS ($z \sim 0$), and include high-redshift star-forming samples from AURORA ($z \sim 1-7$; A. E. Shapley et al. 2025), CEERS ($z \sim 2-6$; R. L. Sanders et al. 2023), and SINS/zC-SINF ($z \sim 1.5-2.5$; N. M. Förster Schreiber et al. 2019a). Theoretical and empirical demarcation lines from L. J. Kewley et al. (2001), K. Schawinski et al. (2007), and G. Kauffmann et al. (2003) are shown in blue, red, and dashed black, respectively. MSA-3D galaxies fall below the AGN boundaries and are consistent with ionization predominantly by young stars in relatively low-metallicity environments from their integrated measurements. [Right] The WHAN diagram (R. Cid Fernandes et al. 2011) showing log([N II]/Hα) *versus* Hα equivalent width for a larger subset of the sample (33 sources) since G140H/100LP grating captures Hα + [N II] for ∼81% of our sample. Nearly all of our galaxies lie well above the EW(Hα) = 3 Å threshold and within the star-forming region, with two sources (MSAIDs: 6848 and 13416) crossing the AGN/Seyfert classification boundary. The six galaxies marked by green circles show the six outflow candidates identified later in Section 3.6.

Nearly all galaxies in our sample lie above the EW(Hα) = 3 Å threshold commonly used to separate star-forming systems from LINER/AGN-dominated sources (R. Cid Fernandes et al. 2011). They occupy the star-forming locus, indicating that their integrated emission-line spectra are governed by H II-region excitation from young stellar populations, with little evidence for quasar-like AGN activity or post-asymptotic giant branch (AGB)-dominated ionization. The two sources (MSAIDs: 6848 and 13416) with log([N II] λ6583/Hα) > −0.5 fall in the "AGN/Seyfert" category and will be revisited later. We emphasize that the WHAN diagram was calibrated on local galaxies, and the higher sSFRs of $z \sim 1$ star-forming systems can shift galaxies toward larger EW(Hα) at fixed [N II]/Hα. For this reason, we do not interpret elevated EW(Hα) by itself as evidence for AGN activity. Our candidate selection of AGNs and outflows relies primarily on enhanced [N II]/Hα together with spatially resolved kinematic disturbances, as discussed in later sections (Section 3.6). The six galaxies marked by green circles show the six outflow candidates identified in our MSA-3D sample.

Next, we construct spatially resolved BPT and WHAN diagrams using the line measurements described in Section 2.2, shown in Figure 3. All analyses use spaxels with S/N > 3 in the required emission lines, i.e., Hα, Hβ, [N II] λ6584, and [O III] λ5007. Individual spaxels are color coded by classification: H II-like (blue), composite/LINER-like (magenta), and Seyfert-like (red) following the L. J. Kewley et al. (2006) diagnostic. While most spaxels cluster in the star-forming region, a nonnegligible fraction (∼11%) of spaxels over the whole sample extends into the "composite/LINER" and AGN-like regions of the BPT diagram, particularly toward higher [O III]/Hβ at fixed [N II]/Hα. A similar trend is seen in the resolved WHAN diagram (Figure 3, right), where most spaxels reside in the star-forming zone, but some extend toward log([N II]/Hα) > −0.4 and EW$_{H\alpha}$ > 3 Å, indicative of transition regions or small, localized zones of shock/AGN or LINER-like excitation. This diversity in spaxel-level excitation is consistent with trends seen in local IFU surveys like MaNGA and CALIFA, where galaxies classified as star-forming in integrated spectra often reveal central regions with low-luminosity AGN (LLAGN)-like excitation and/or shock-driven ionization or emission from evolved stars near the outskirts (F. Belfiore et al. 2016; D. Wylezalek et al. 2018; N. Roy et al. 2021a). While these zones typically occupy only a small area (<5 kpc^2) of the galaxy, their detection in the resolved BPT and WHAN diagrams highlights the importance of spatial resolution: such weak, compact ionization sources are completely diluted in integrated light.

3.3. Spatially Resolved Line Emission

With JWST, we now obtain spatially resolved rest-frame optical spectroscopy for statistically meaningful samples of galaxies, enabling a robust dissection of their internal structure. From subkiloparsec maps, we can jointly trace ionized-gas excitation and kinematics, nebular abundances, and stellar continuum, yielding a physically coherent view of the gas and stars within each system. Figure 4 shows example maps of two galaxies from our sample in the two rows. For each galaxy, we display the HST F160W image, continuum map, Hα, and [N II] flux maps where the S/N of each of the emission lines shown is greater than 3. These two example systems are representative of the diverse nature in the line-emitting gas that is found in the entire sample. The top row presents a galaxy that shows a clumpy and irregular ionized-

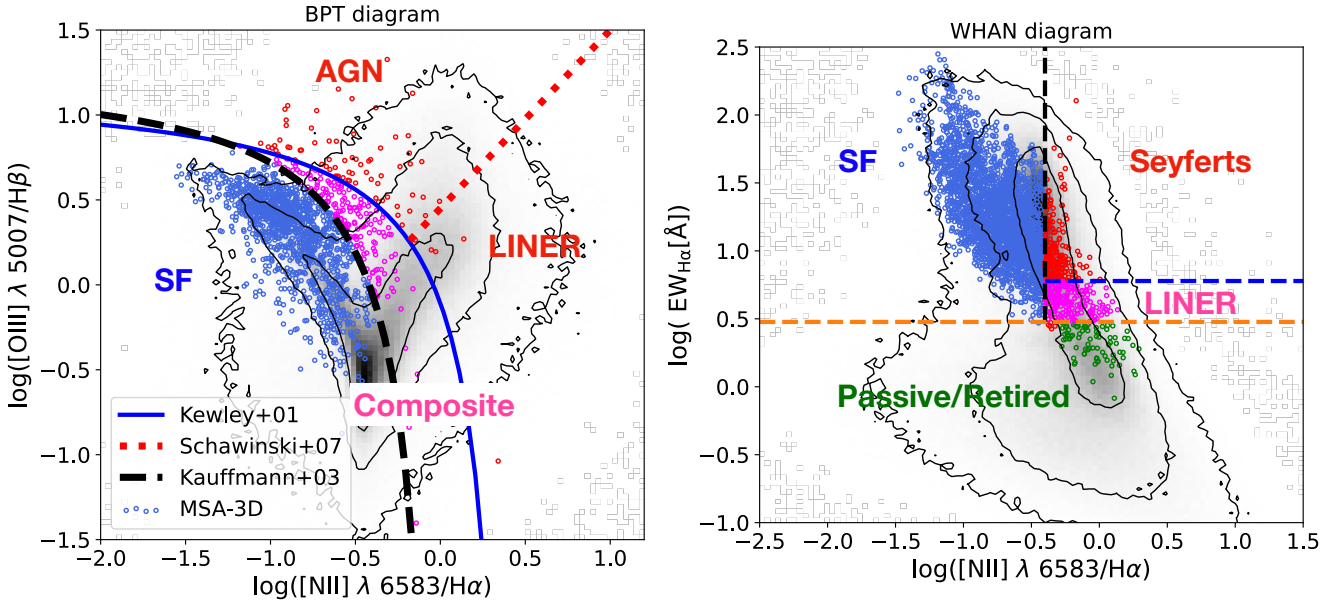


Figure 3. Spatially resolved emission-line diagnostics for the MSA-3D sample. (Left) The BPT diagram and (right) WHAN diagram for individual spaxels for all MSA-3D galaxies. Displayed spaxels satisfy S/N > 3 for each of Hα, Hβ, [N II] λ6584, and [O III] λ5007, and any spaxels below this threshold in any line are masked. The flux measurements are obtained from line fitting, following the procedure described in Section 2.2. Spaxels are color coded by their excitation mechanism based on the L. J. Kewley et al. (2001) and G. Kauffmann et al. (2003) diagnostics: the star formation or H II-region-like in blue, AGN and Seyfert-like in red, and the composite ionization or LINER source in magenta. While the majority of spaxels occupy the star-forming locus, a nonnegligible subset of spaxels extend into the composite/LINER and AGN-like regimes. This indicates that AGN, shocks, and mixed-ionization sources can be missed in integrated spectra. Sensitive, spatially resolved spectroscopy is required to detect and disentangle these components.

gas distribution, but the stellar continuum shows a disklike, centrally concentrated but elongated structure. However, the nebular emission lines exhibit knots and patches, which are indicative of localized star-forming regions. Interestingly in this galaxy, the ionized gas shows two distinct peaks, which are not spatially coincident with the peak of the stellar continuum. It is possible that dust is obscuring parts of the ionized gas, making the distribution appear clumpy. About $\sim$40% of the MSA-3D sample has clumpy, patchy ionized-gas morphology resembling the galaxy at the top row.

In contrast, the bottom row shows a galaxy with a much smoother and more centrally concentrated distribution in both the continuum and emission lines. Here, the gas and stars are largely spatially coincident, with emission from Hα, and [N II] following the same overall morphology as the stellar light. This suggests a more uniform star-forming disk, where ionized gas closely traces the stellar mass distribution. The diversity in gas morphology is as follows: from disturbed, clumpy gas distribution to smooth, disklike structures, it provides important clues about the processes shaping SF and feedback at $z \sim 1$. To further understand how these variations manifest in the physical conditions of the gas, we now turn to the radial behavior of key emission-line ratios across our sample.

3.4. Radial Gradients in Emission-line Ratios

Spatially resolved emission-line ratios provide powerful diagnostics of the physical conditions within the ISM, offering insight into gas-phase metallicity, ionization parameter, and the hardness of the ionizing radiation field. Radial gradients in key line ratios—such as [N II]/Hα, [S II]/Hα, [O III]/Hβ, and [N II]/[S II]—probe the combination of the above quantities and trace the interplay between chemical enrichment, SF, feedback processes, and gas accretion over cosmic time (S. Sánchez et al. 2015; R. Maiolino & F. Mannucci 2019). These diagnostics capture how galaxy ISM properties evolve due to their past SF history and ongoing baryon cycling within the disk.

For each galaxy in our sample of 38 MSA-3D sources, we compute the spaxel-by-spaxel line ratios [N II]/Hα, [N II]/[S II], [S II]/Hα, and [O III]/Hβ. Here, we do not impose any S/N cut on any of the emission lines, to avoid biasing the line ratios toward only the brightest line-emitting regions. We compute deprojected radial distances for each spaxel and normalize by the effective radius (R/R_e). These per-spaxel flux measurements are grouped into annular bins of equal radial width. We then construct radial profiles by computing the S/N-weighted mean flux of each emission line within each annulus and taking the ratio of these annulus-averaged line fluxes. This differs from an integrated profile, where one would first coadd the spectra within each annulus and then measure the line ratios on the resulting integrated spectrum. Figure 5 illustrates an example radial profile of a representative galaxy from our sample. The gray points indicate individual spaxel measurements as a function of R/R_e, while the magenta markers show the mean values in the radial bins. We adopt this binned radial profile methodology throughout the paper to characterize radial variations in excitation and abundance-sensitive line ratios. Figure 6 presents the full set of binned radial profiles for the entire sample. Individual galaxy radial trends are shown in gray, while the median profiles for the high-mass ($\log M_\star \geqslant 9.8\, M_\odot$) and low-mass ($\log M_\star < 9.8\, M_\odot$) bins are overplotted in red and blue, respectively. Error bars show the standard error of the mean across galaxies in each radial bin. We also fit linear trends to the median profiles, shown in magenta and cyan for the high- and low-mass bins, respectively, to quantify the radial gradients of the median relations. For comparison, we overlay the mean radial gradients (with 1σ scatter) observed in star-

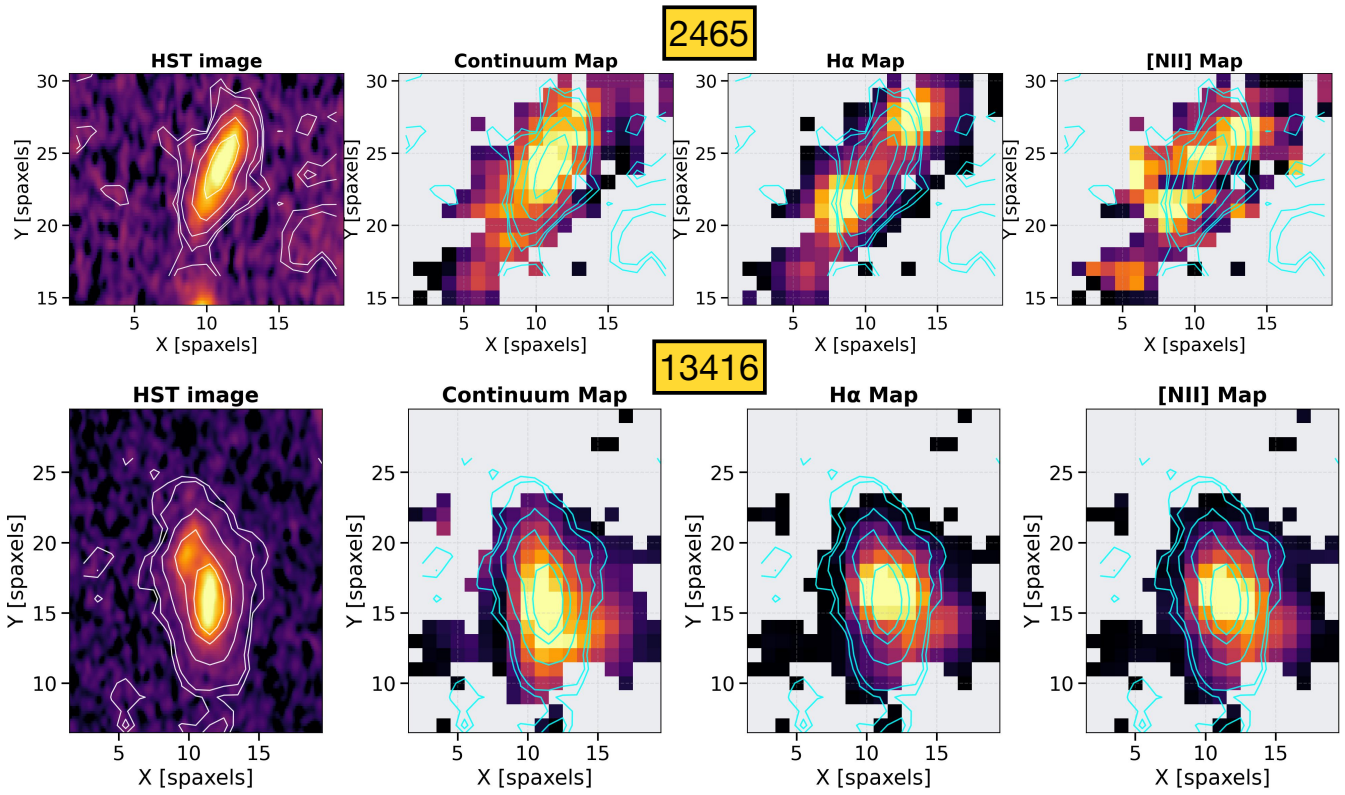


Figure 4. Example two-dimensional maps for two representative galaxies (one in each row) from the MSA-3D sample, demonstrating the spatially resolved data quality achieved with the NIRSpec slit-stepping strategy. For each galaxy (top, ID 2465; bottom, ID 13416), the panels from left to right show: (1) the HST/WFC3 F160W image; (2) the rest-optical continuum map derived from the IFU data cube by masking strong emission lines and summing along the spectral axis; (3) the Hα flux map; and (4) the [N II] λ6584 flux map. Emission-line fluxes are measured by Gaussian fits to individual spaxels that satisfy our S/N detection thresholds for all required lines, as detailed in Section 2.2. Overplotted contours trace the stellar morphology from the HST image, to enable direct spatial comparison. These examples highlight the morphological diversity in the ionized-gas distribution across the MSA-3D sample. We encounter galaxies with well-ordered, disklike Hα emission aligned with the stellar distribution (similar to 2465), while a few sources show clumpy and offset ionized-gas structures (13416). These reflect variations in gas excitation, kinematics, or dust geometry across the galaxy.

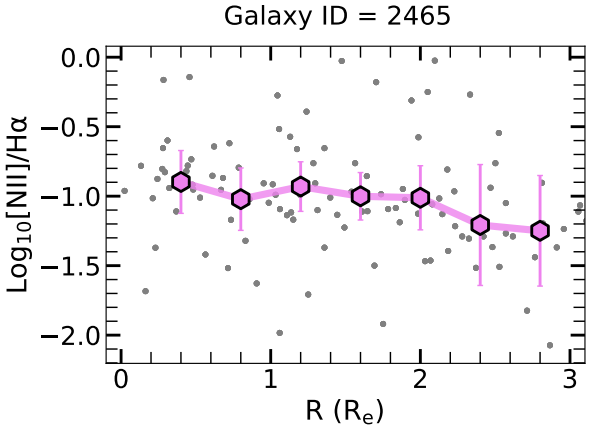


Figure 5. Radial profile of log([N II]/Hα) emission-line ratio for a representative galaxy from our sample. We compute the deprojected radial distances for each spaxel and normalize by the effective radius (R/R_e). Gray points indicate the line ratio measurements for each individual spaxel, while magenta hexagons denote the mean values of the nebular ratio, computed within annular radial bins of equal width. We adopt this binned radial profile methodology, described in Section 3.4, to characterize radial variations in ionization and abundance-sensitive line ratios.

forming galaxies at $z \sim 0$ from the MaNGA survey (F. Belfiore et al. 2016; yellow-shaded region).

The [N II]/Hα ratio serves as a widely used proxy for gas-phase metallicity, as the nitrogen-to-hydrogen abundance scales with oxygen abundance in metal-rich environments, with some modest dependence on the ionization parameter (L. J. Kewley & M. A. Dopita 2002). In our sample (Figure 6, top left), the mass-averaged profile of log([N II]/Hα) for the high-mass bin (red) is consistent with a flat gradient, with a best-fit slope consistent with zero (slope $<0.001 \pm 0.001$ dex Re^{-1}). Individual systems (shown in gray) nevertheless show mildly negative trends. A dedicated metallicity-gradient analysis of the MSA3D sample by M. Ju et al. (2025) likewise finds mostly flat to negative gradients, with dZ/dr spanning -0.03 to $+0.02$ dex kpc^{-1}, in agreement with our results. A coherent picture emerges in which metallicity gradients steepen (become more negative) with increasing stellar mass, plausibly because more massive, disk-dominated systems retain and imprint inside-out enrichment, and this trend agrees with theoretical models that include strong stellar feedback (X. Ma et al. 2017; Z. S. Hemler et al. 2021). We refer the reader to M. Ju et al. (2025) for more detailed discussion on metallicity gradients. We do note that the local galaxies ($z \sim 0$, shown in yellow) show a stronger negative gradient and higher absolute metallicities compared to our $z \sim 1$ systems, consistent with continued cosmic enrichment relative to our higher-redshift sample.

The [S II]/Hα ratio, while sometimes used as a secondary metallicity indicator, is more sensitive to the ionization structure and gas-phase conditions within the ISM, particularly in the partially ionized regions. This ratio is especially effective in distinguishing emission from classical H II regions and low-ionization (LI(N)ER-like) excitation. Our sample

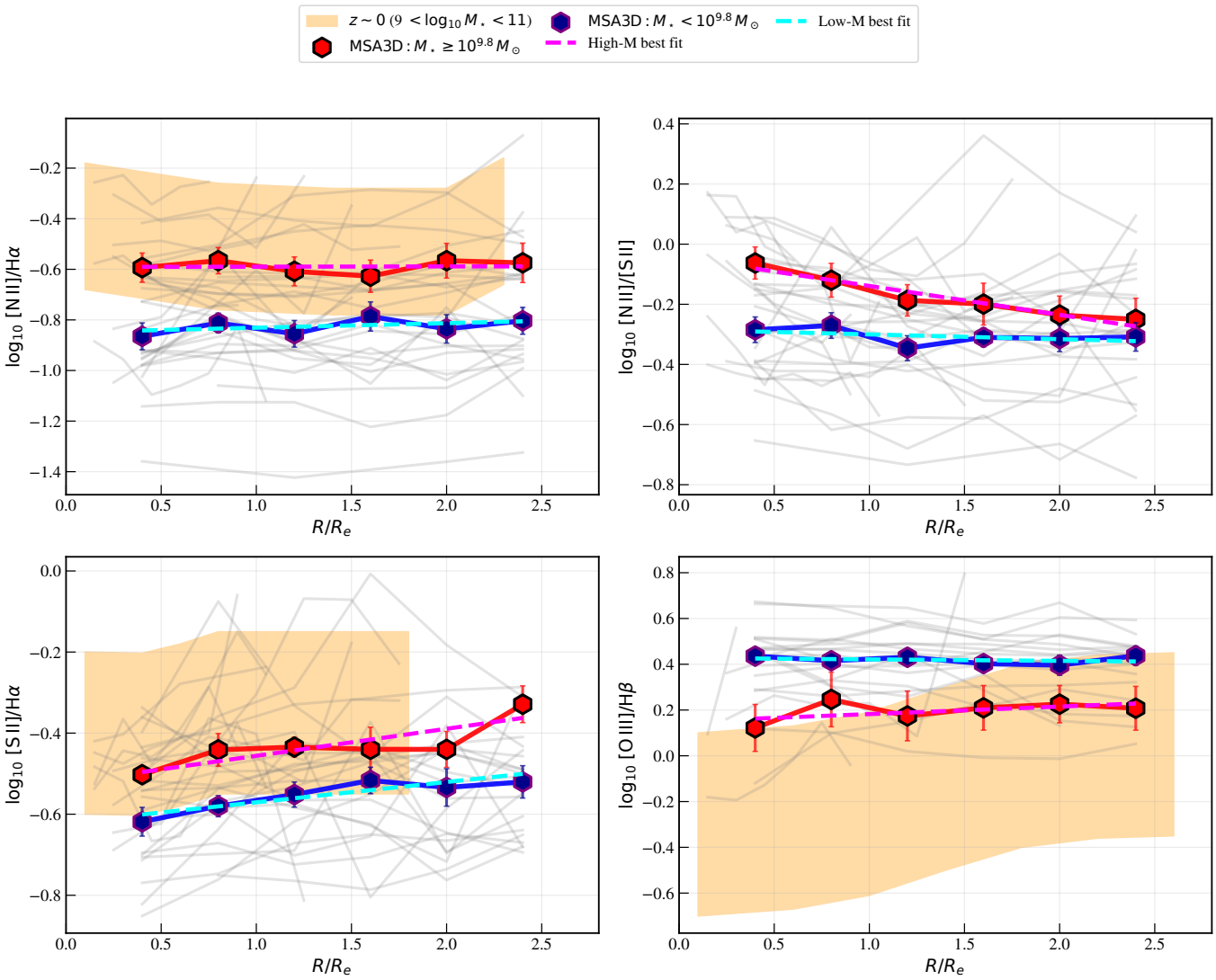


Figure 6. Binned radial profiles for four emission-line ratios across the entire MSA-3D sample: log ([N II]/Hα) [top left], log ([N II]/[S II]) [top right], log ([S II]/Hα) [bottom left], and log ([O III]/Hβ) [bottom right]. Individual galaxy-binned radial trends, computed by the method described in Section 3.4, are shown in gray. The blue and the red denote the median profiles for the high-mass ($\log M_\star \geqslant 9.8$) and low-mass ($\log M_\star < 9.8$) galaxies, respectively. For comparison, the yellow-shaded regions indicate the mean radial gradients with 1σ scatter observed in star-forming galaxies at $z \sim 0$ from the MaNGA survey (F. Belfiore et al. 2016). The MSA-3D galaxies exhibit systematically lower [N II]/Hα and [S II]/Hα ratios and elevated [O III]/Hβ compared to $z \sim 0$ MaNGA star-forming galaxies, reflecting their lower metallicities and more extreme ionization conditions at $z \sim 1$. The detailed description on the radial trends and their implications are discussed in the text.

shows a mean log([S II]/Hα) ~ -0.5 for the more massive galaxies and ~ -0.6 for lower-mass systems. These values are broadly consistent with ionization from young stars in typical star-forming regions. For comparison, F. Belfiore et al. (2016) reported a mean value of log([S II]/Hα) ~ -0.4 for star-forming regions in $z \sim 0$ galaxies, with a clear separation from LINER-like systems, which exhibit elevated values of log([S II]/Hα) ~ -0.1. The nebular emission in our sample is thus consistent with SF-driven ionization.

The [S II]/Hα ratio shows a clear positive radial gradient, with best-fit slopes of (0.050–0.067) ± 0.016 dex R_e^{-1}. Although [S II]/Hα is sometimes used as a secondary metallicity diagnostic, it is also sensitive to the ionization state and density structure of the gas. In local galaxies, an outward increase in [S II]/Hα is commonly associated with a growing contribution from diffuse ionized gas (DIG), since DIG typically exhibits enhanced low-ionization forbidden-line emission relative to Hα compared to classical H II regions (F. Belfiore et al. 2016; R. L. Sanders et al. 2017; K. Zhang et al. 2017). A similar trend can also arise if the ionization parameter decreases with radius, such that the outer disk becomes progressively less dominated by compact, high-ionization star-forming regions (K. Zhang et al. 2017; E. A. D. Lacerda et al. 2018). Figure 6 (top right) shows that the [N II]/[S II] ratio, on the other hand, exhibits a negative radial gradient, with slopes of -0.096 ± 0.013 dex R_e^{-1} in the high-mass bin and -0.016 ± 0.011 dex R_e^{-1} in the low-mass bin. Since [N II]/Hα remains nearly flat with radius, the decline in [N II]/[S II] is effectively driven by the same outward increase in [S II]/Hα, and the two trends are different manifestations of the same underlying radial change in the ionized-gas conditions. [N II]/[S II] is often used as a proxy for N/S and, approximately, N/O, because sulfur is an α element that broadly tracks oxygen, while nitrogen acquires a stronger secondary component at higher metallicity. A declining [N II]/[S II] ratio toward larger radii therefore suggests that the

outskirts are less nitrogen enhanced than the inner regions, consistent with weaker secondary nitrogen production and inside-out chemical enrichment. Our interpretation is consistent with local benchmarks. D. A. Berg et al. (2020) report similarly negative radial gradients in N/O for nearby galaxies and attribute them to the delayed, largely secondary production of nitrogen in intermediate-mass stars, in contrast to the prompt α-element yields (O and S) from core-collapse supernovae. Thus, the outward rise in [S II]/Hα and the decline in [N II]/[S II] most likely reflect a combination of changing ionization conditions and radial abundance-ratio gradients. The outer regions likely have a larger DIG contribution and lower ionization parameter, which boosts [S II]/Hα, while also showing lower N/S, and approximately lower N/O, than the center of the galaxies. We finally note that shocks and low-level outflows can further boost [S II]/Hα, and we present such examples on a case-by-case basis in later sections.

Figure 6 (bottom right panel) shows the [O III]/Hβ ratio, which is another diagnostic that depends on ionization parameter, hardness of the radiation field, and also gas-phase metallicity. Lower-metallicity environments typically host hotter, younger stellar populations with harder ionizing spectra and less efficient cooling, which enhance [O III] emission relative to Balmer recombination lines. Our sample exhibits a clear mass dependence: low-mass galaxies show elevated [O III]/Hβ ratios with mean log ([O III]/Hβ) $\sim$0.4, and higher-mass galaxies lie systematically lower at a mean of 0.1. This trend is consistent with previous findings that low-mass galaxies at high redshift are both less chemically evolved and tend to host more extreme ionization conditions, which is further supported by the lower [N II]/Hα in the BPT diagram (R. L. Sanders et al. 2021; M. Curti et al. 2023).

The radial profiles of [O III]/Hβ in our sample are generally flat to mildly rising, with a best-fit slope of 0.0329 ± 0.0228 dex $R\mathrm{e}^{-1}$ for the high-mass bin. Although only marginally positive, this behavior is expected in systems with flat or mildly negative metallicity gradients, as lower metallicity reduces cooling, raises the electron temperature, and boosts the [O III]/Hβ ratio at larger R/R_e. So this is consistent with the O/H gradients discussed by M. Ju et al. (2025). Comparable flat or weakly positive [O III]/Hβ gradients have been reported in both local galaxies and high-redshift samples (F. Belfiore et al. 2017; D. Kashino et al. 2017; A. Claeyssens et al. 2023; R. L. Sanders et al. 2023). A more comprehensive analysis of gas-phase metallicity gradients and their stellar mass dependence in the MSA-3D sample is presented in M. Ju et al. (2025). We note that [O III]/Hβ also responds to the ionization parameter (U) and spectral hardness. A systematic decrease of U with radius would tend to lower [O III]/Hβ, while harder radiation fields or leakage can counteract this effect. Altogether, these results indicate that the processes shaping metal production, transport, and ionization structure are already well established by $z \sim 1$, when they are still assembling their stellar mass and metal reservoirs.

3.5. ***Kiloparsec***-scale Spatially Resolved Correlation between [N II]/Hα and Velocity Dispersion

Radial gradients of emission-line ratios, discussed in the previous section, provide important constraints on how gas-phase metallicity, excitation, and ISM conditions evolve with galactocentric distance. However, spatially resolved, spaxel-by-spaxel diagnostics can uncover more localized physical processes. Here, we investigate the spatially resolved connection between the nebular line ratios, [N II]/Hα and [O III]/Hβ, that are sensitive to both metallicity and ionization and the ionized-gas velocity dispersion (σ), which reflects the dynamical state of the gas and can be elevated by turbulence, shocks, or feedback-driven motions.

Figure 7 shows the distribution of individual spaxels from the full MSA-3D sample in the BPT-σ and WHAN-σ planes. We include every spaxel with S/N > 3 for each of Hα, Hβ, [N II] λ6584, and [O III] λ5007, irrespective of its galactocentric location. A clear positive correlation emerges: higher-velocity dispersion coincides with elevated [N II]/Hα in the WHAN diagram, while low-σ regions tend to show lower line ratios. Part of this trend likely reflects the resolved mass–metallicity relation seen at both low and high redshift (F. F. Rosales-Ortega et al. 2012; A. G. Sánchez et al. 2013), where regions of higher stellar surface density host more metal-enriched gas. Since stellar mass surface density correlates with kinematics (M. Cappellari et al. 2006), high-σ regions naturally map to higher metallicity and thus higher [N II]/Hα.

However, deviations from this baseline can arise where shocks, outflows, or LLAGN locally boost both σ and the excitation state. In particular, spaxels with elevated σ that fall in Seyfert/AGN loci of the BPT/WHAN diagnostics likely trace compact, energetically active zones embedded within otherwise star-forming disks. Indeed, we see spaxels classified as AGN from the BPT/WHAN typically exhibit higher σ. These spatially resolved diagnostics therefore provide a sensitive means to uncover weak, low-surface-brightness nonstellar excitation that would be diluted in integrated spectra. A comprehensive analysis of emission-line kinematics for the full sample will be presented in a follow-up paper (Espejo Salcedo et al. 2026, in preparation). Here, we identify sources hosting spaxels with high σ, enhanced log ([N II]/Hα), and lying in the AGN/Seyfert classifications in the BPT or WHAN diagrams, and discuss them on a case-by-case basis below.

3.6. Case Studies: Candidates with Possible Weak AGN Activity

We demonstrate in Figure 2 that the MSA-3D sample predominantly includes typical star-forming galaxies with young, OB stars from H II regions largely contributing to the ionization of the ISM. Only two galaxies with IDs 11843 and 13416 are consistent with AGN/LINER-like excitation from the integrated WHAN/BPT (log([N II]/Hα) > -0.4) in the $2R_\mathrm{e}$ aperture-summed spectrum. These two galaxies stand as candidates featuring ionization signatures of either LLAGN activity or shocked gas from centrally driven gas outflows.

However, Figure 3 demonstrates that spatially resolved spectroscopy can reveal localized signposts of weak AGN activity, shocks, or disturbed gas that would remain diluted in integrated spectra. We therefore study each galaxy on a case-by-case basis and look for spatially coherent regions with at least three contiguous significant spaxels with nonstellar or mixed line ratio classifications, disturbed ionized-gas kinematics, and offsets from regular disk geometry and kinematics.

We compute the observed second velocity moment of the ionized gas, $V_\mathrm{rms} = \sqrt{v^2 + \sigma^2}$, where v is the line-of-sight

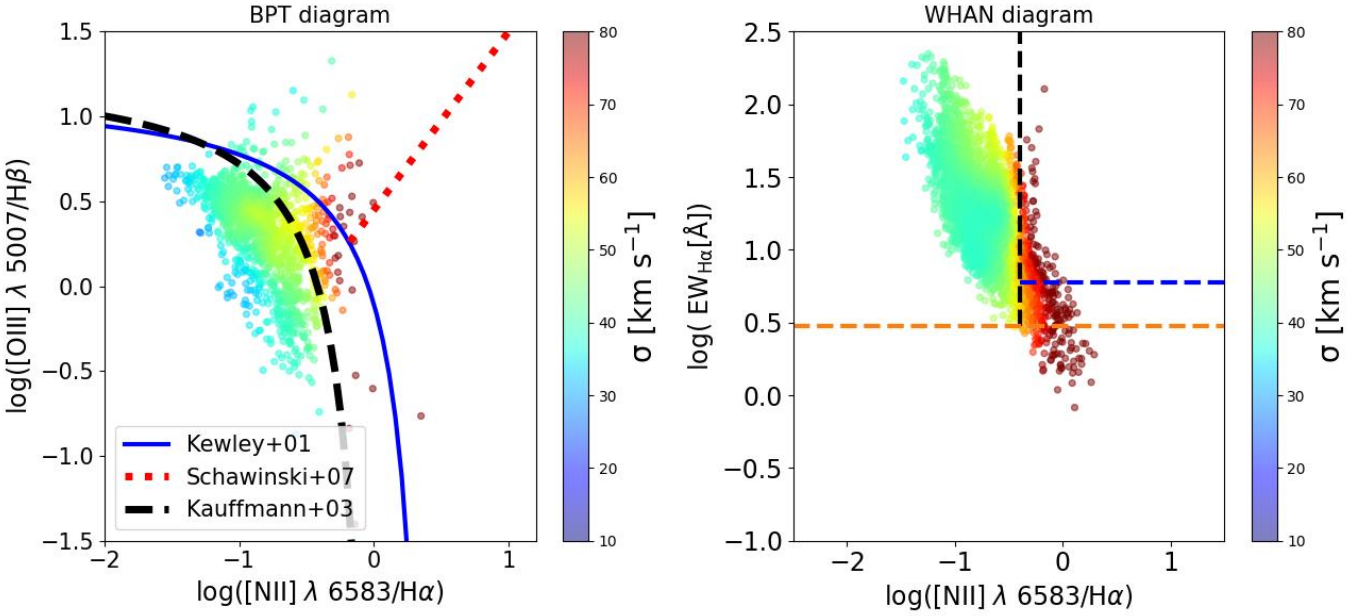


Figure 7. Spatially resolved BPT (left) and WHAN (right) diagrams color coded by velocity dispersion (σ) for all spaxels in the MSA-3D sample with S/N of the required emission lines > 3. We observe a clear increase of [N II]/Hα with σ, consistent with enhanced excitation in high-dispersion regions. Elevated σ is often associated with shocks, outflows, or AGN photoionization, and they preferentially lie in the Seyfert/AGN loci in both diagrams. This spaxel-by-spaxel view reveals weak, locally confined (low-surface-brightness) nonstellar excitation embedded within otherwise star-forming galaxies.

velocity offset from the systemic redshift measured from the Hα fits, and σ is the Gaussian velocity dispersion corrected for instrumental broadening. Since beam smearing can enhance the apparent dispersion near galaxy centers, we do not use $V_{\rm rms}$ alone as evidence for outflows. Instead, elevated $V_{\rm rms}$ and σ are used as empirical flags for identifying possible dynamically disturbed regions. The advantage of the resolved MSA-3D data is that these kinematic signatures can be assessed in their spatial context. We therefore interpret elevated second moments only when they are spatially coherent and considered together with line ratio structure, gas morphology, kinematic-axis misalignment between stellar and gas disks, and asymmetric or multicomponent line profiles where present.

We impose S/N > 3 in all constituent lines (including [N II] and Hβ) to ensure that our line ratio and σ measurements and their uncertainties are reasonable. Errors in line ratios are computed by standard error propagation of the individual line flux errors. Following these criteria, we find six candidate systems hosting weak AGN activity, shocks, or outflows. For the candidate systems, we also inspected the spectra from the highest-σ regions using one- and two-component fits to evaluate whether a second kinematic component is required. Clear multicomponent structure is detected in three out of six candidates, while the remaining systems are adequately described by a single dominant component at the spectral resolution and S/N of the current data. In this section, we present all those six cases in detail along with a pure star-forming galaxy as a comparison source.

3.6.1. ID: 2465—A Purely Star-forming Galaxy

Figure 8 presents spatially resolved diagnostics of a representative example of a star-forming system (ID: 2465). The top row displays the HST F160W imaging and resolved ionized-gas properties—the Hα flux, line-of-sight velocity field, and velocity dispersion map obtained from Gaussian fits to the Hα line (see Section 2.2 for details). The bottom row shows (i) the WHAN diagram constructed from all spaxels, (ii) the spatial location of those spaxels in the galaxy, color coded by their WHAN classification, (iii) the second velocity moment ($V_{\rm rms} = \sqrt{v^2 + \sigma^2}$), and (iv) the H$\alpha$ equivalent width (EW) map. Spaxels are color coded and categorized according to their position in the WHAN diagram based on log([N II]/Hα) and Hα EW:

1. log([N II]/Hα) < -0.7 and EW$_{\rm H}\alpha > 3$ Å, blue (pure star-forming);
2. $-0.7 \leqslant$ log([N II]/Hα) < -0.5 and EW$_{\rm H}\alpha > 3$ Å, cyan (SF-intermediate);
3. $-0.5 \leqslant$ log([N II]/Hα) < -0.4 and EW$_{\rm H}\alpha > 3$ Å, pink (transition zone);
4. log([N II]/Hα) $\geqslant -0.4$ and $3 <$ EW$_{\rm H}\alpha < 6$ Å, magenta (LI(N)ER-like);
5. log([N II]/Hα) $\geqslant -0.4$ and EW$_{\rm H}\alpha > 6$ Å, red (AGN/shock dominated).

We interpret the blue spaxels as tracing classical H II regions ionized by young, bright OB stars, while red spaxels are likely associated with AGN or fast radiative shocks. Magenta spaxels may reflect LI(N)ER-like excitation from evolved stellar populations (e.g., post-AGB stars) or slow moving shocks. Cyan and pink regions represent intermediate regimes transitioning from SF to harder ionizing sources.

In the case of galaxy 2465, over 92% of spaxels fall into the blue or cyan categories, which suggests that the ionization is dominated by photoionization from star-forming regions. The few pink/magenta/red spaxels do not form coherent structures ($\leqslant$3 contiguous spaxels) and fail to meet our criteria for physical significance. Those may arise from noise or fitting artifacts. The gas kinematics give additional clues regarding the nature of this system. The ionized-gas velocity field looks smooth and symmetric, consistent with ordered rotation. The kinematic major axis from the Hα velocity field is aligned with

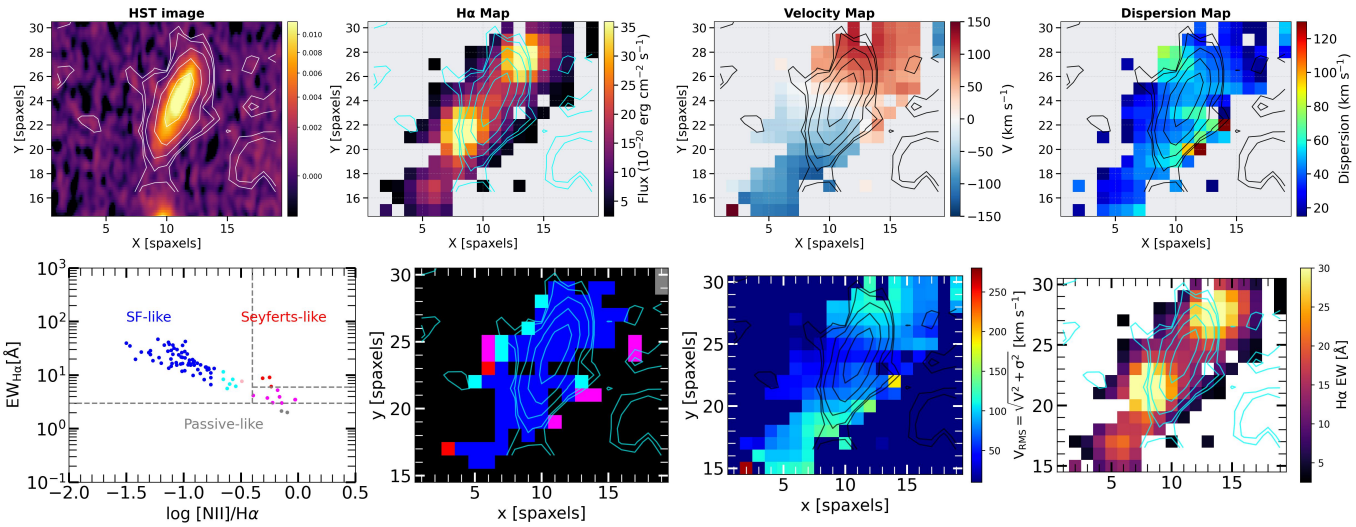


Figure 8. Detailed maps and spatial diagnostics of a purely star-forming galaxy (ID: 2465). Top row (left to right): the HST F160W image, Hα flux map, ionized-gas (Hα) velocity field, and velocity dispersion map derived from Gaussian fits to a Hα emission line. Cyan and black contours trace stellar isophotes from the HST image. Bottom row: [left] the WHAN diagram showing individual S/N > 3 spaxels color coded by ionization class, star-forming (blue), Seyfert-like (red), LINER-like (magenta), and passive (gray), based on the [N II]/Hα ratio and Hα equivalent width. Cyan and pink colors represent intermediate/transition zones bridging the purely star formation regions to AGNs/LINERs. [Second from left] The distribution of the color coded spaxels projected on the galaxy. [Third from left] 2D map of the second velocity moment: $V_{\rm rms} = \sqrt{v^2 + \sigma^2}$, which represents the dynamic motion of the gas. [Right] Hα equivalent width (EW) map. Over 92% of spaxels in this galaxy fall into the blue or cyan categories, which suggests that the ionization is dominated by photoionization from star-forming regions. The ionized-gas velocity field looks smooth and symmetric with $V_{\rm rms} < 100$ km s^{-1}. Hence, the gas kinematics is consistent with ordered rotation in a purely star-forming disk galaxy.

the stellar disk seen in the HST image. The measured velocity dispersion ($\sigma \leqslant 65$ km s^{-1} and $V_{\rm rms} \leqslant 130$ km s^{-1}) is modest, further supporting a dynamically settled disk in which ordered rotation dominates over disordered motion. We therefore classify this system as a purely star-forming galaxy with no evidence for AGN activity or kinematically disturbed gas from outflows/shock-heated gas.

3.6.2. IDs: 9960 and 6848—Low-luminosity AGNs Driving Outflows

We now present spatially resolved emission-line diagnostics for candidates that exhibit signatures of AGN activity and disturbed ionized-gas kinematics due to outflows. Figure 9 displays the maps for galaxy ID 9960, where the panels and the symbols are as in Figure 8. The HST imaging suggests an inclined disk, yet the line-of-sight kinematics—peak velocities ($v \geqslant 150$ km s^{-1}) and dispersions ($\sigma \geqslant 120$ km s^{-1})— indicate a dynamically disturbed, highly energetic system rather than a smooth rotating disk. Although a BPT diagram cannot be constructed because [O III] λ5007 falls within a detector chip gap, we instead employ the WHAN diagnostic. It is to be noted that this galaxy was classified as fully star-forming from the integrated WHAN diagram, shown in Figure 2.

The spatial distribution of WHAN-classified spaxels reveals a central concentration of AGN-like excitation (red), surrounded by pink and magenta spaxels that are more consistent with mixed excitation from evolved stars and shocks or transition-like excitation. In particular, the spatially extended pink spaxels are likely more relevant for the disturbed outer regions and may reflect a combination of AGN photoionization and shock excitation, rather than a single ionization source, similar to those seen in $z \sim 0$ galaxies (F. Belfiore et al. 2016; N. Roy et al. 2018, 2021a). We therefore interpret the resolved line ratio structure in this source as evidence for mixed excitation associated with a weak AGN and disturbed outflowing gas.

The kinematic maps reveal strongly disturbed gas dynamics. Regions of high-velocity dispersion ($\sigma \sim$ 120–140 km s^{-1}) extend across the system and coincide spatially with spaxels exhibiting non-star-forming ionization. These spaxels outline an extended conical structure oriented roughly perpendicular to the stellar disk. A major part of the galaxy also has $V_{\rm rms} \geqslant 300$ km s^{-1}. These values are well above those expected for purely rotation-supported disks and are inconsistent with gravitational motions alone. Additionally, we detect a secondary broad component in the emission lines, with line widths exceeding $>$500 km s^{-1}, as shown in Figure 10. These signatures together point to the presence of high-velocity, turbulent outflows driven from the central, weak AGN.

In fact, it is not unusual for local low-luminosity Seyfert galaxies to have extended ionized gas with LINER-like ratios, indicative of shocks in an outflow (J. Xia et al. 2018). These observed properties are also similar to the so-called "red geysers" identified in the MaNGA survey, which are passive, elliptical galaxies displaying large-scale biconical outflows (E. Cheung et al. 2016; N. Roy et al. 2018, 2021a). They show similarly elevated σ and $V_{\rm rms}$ values (typically $V_{\rm rms} \gtrsim 200$ km s^{-1}) and widespread LINER emission attributed to AGN-driven winds (N. Roy et al. 2018, 2021a, 2021c). Galaxy 9960 may represent a high-redshift analog of such systems exhibiting AGN-driven outflows, albeit with nonnegligible SF.

Galaxy 6848, on the other hand, presents a compelling case with a compact ionized-gas morphology dominated by a nonstellar ionization mechanism. Over 95% of the resolved spaxels fall within the Seyfert regime in the WHAN diagram as shown in Figure 11, making it the most AGN-dominated source in our sample in terms of areal coverage. This galaxy also falls in the AGN/Seyfert category in the integrated WHAN diagram (Figure 2). Unlike more extended systems

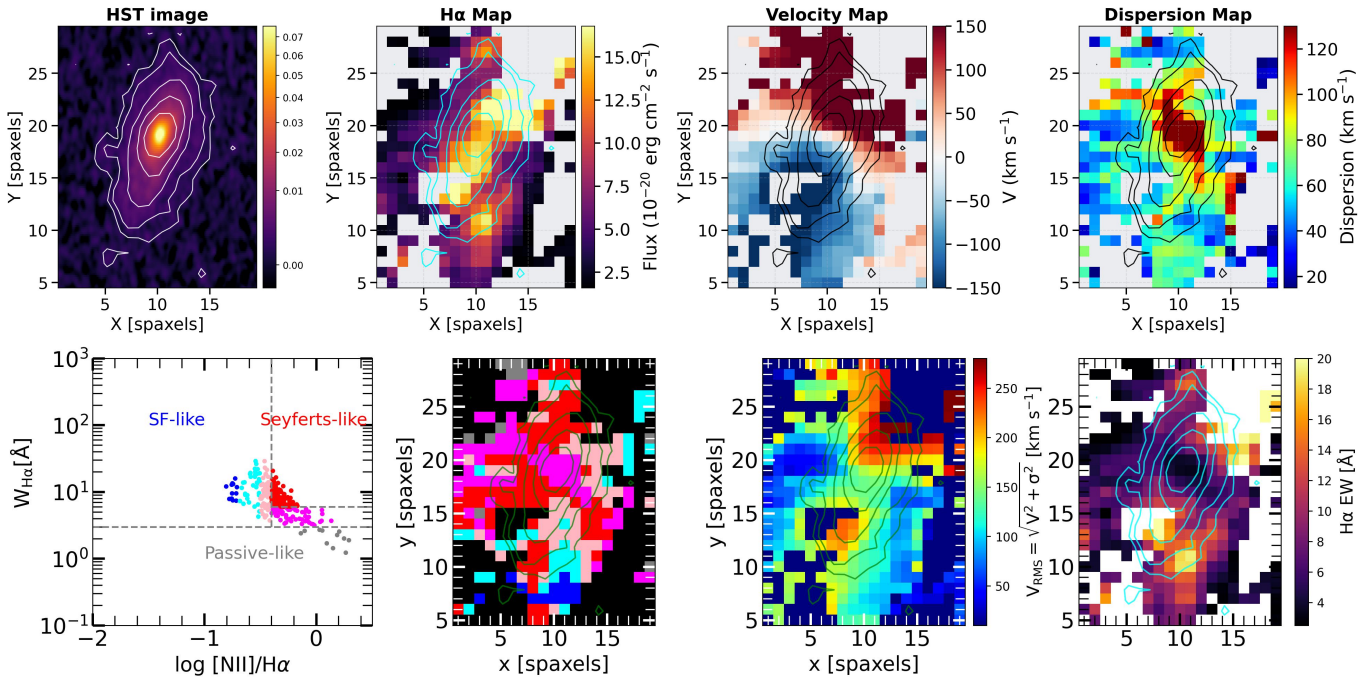


Figure 9. Spatially resolved maps for galaxy 9960. The panel layout and diagnostics shown are identical to those in Figure 8. The HST image suggests an inclined disk, but the velocity and dispersion maps reveal disturbed ionized gas, and the high-σ regions outline a roughly biconical structure projected approximately perpendicular to the disk. WHAN-classified spaxels show a concentration of AGN/LINER-like and mixed excitation that is roughly cospatial with elevated velocity dispersion. This spatial coincidence is suggestive of noncircular or outflowing gas, although shocks, stellar-feedback-driven motions, or nongravitational disturbances may also contribute to these observed signatures.

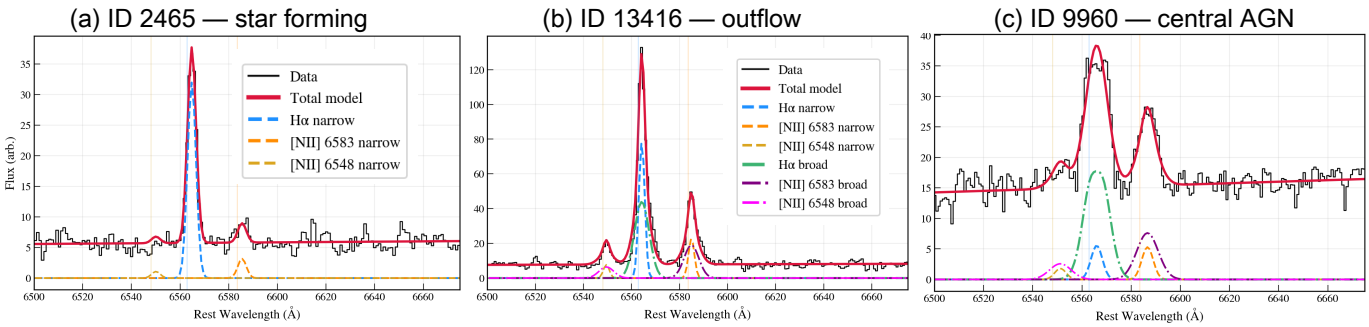


Figure 10. Rest-frame optical spectra illustrating the diversity of nebular kinematics. Left: an emission-line profile of Hα+[N II] in galaxy 2465, extracted from the central 3 × 3 spaxels. The line profile shows a narrow, symmetric shape consistent with typical star-forming H II regions dominated by rotating disk kinematics. Middle: an emission-line profile for galaxy ID 13416, extracted from a 3 × 3 spaxel box, coincident with the outflow location, possibly driven by supernovae. The spectral profile shows a pronounced wing, requiring an additional kinematic component, commonly associated with bulk outflow/inflow. The two-component fit is shown. Right: a broad emission-line feature (line width $\gtrsim$ 500 km s^{-1}) indicative of AGN-driven outflow gas in galaxy 9960. All spectra are continuum subtracted, arbitrarily flux normalized, and shifted to rest wavelength.

such as galaxy 9960, where shock-excited spaxels trace an extended conical pattern, here, they are centrally concentrated, but span the full extent of the detectable ionized gas. The galaxy exhibits strong Hα luminosity across its compact extent, suggesting a dense and highly ionized environment. Although the IFU data reveal a relatively small spatial footprint with sufficient S/N in Hα and [N II], HST imaging shows faint, low-surface-brightness features extending beyond the Hα morphology. This implies that the true extent of the ionized gas is likely larger, but falls below the S/N threshold of the MSA-3D observations. Kinematically, the gas shows moderate turbulence, with velocity dispersions reaching $\sigma \gtrsim 120\,\mathrm{km\,s^{-1}}$ and second velocity moments (V_{rms}) exceeding $150\,\mathrm{km\,s^{-1}}$ in the central region. A comparison of one- and two-component fits to the extracted spectra from the disturbed regions shows that a second Gaussian component is statistically preferred, indicating that the line profile cannot be fully described by a single kinematic component. This provides further evidence of AGN-regions possibly driving an outflow.

3.6.3. IDs: 13416 and 12015—Galaxies with Off-nuclear Outflow or Shock Signatures

Galaxy 13416 is the other source in our sample, besides 6848, that falls in the non-star-forming regime in the integrated WHAN/BPT diagnostics, with a global log([N II]/Hα) > -0.4 (Figure 2). The spatially resolved WHAN diagram in Figure 12 shows that approximately 80% of spaxels fall in the AGN/LINER or transitional loci (color coded as

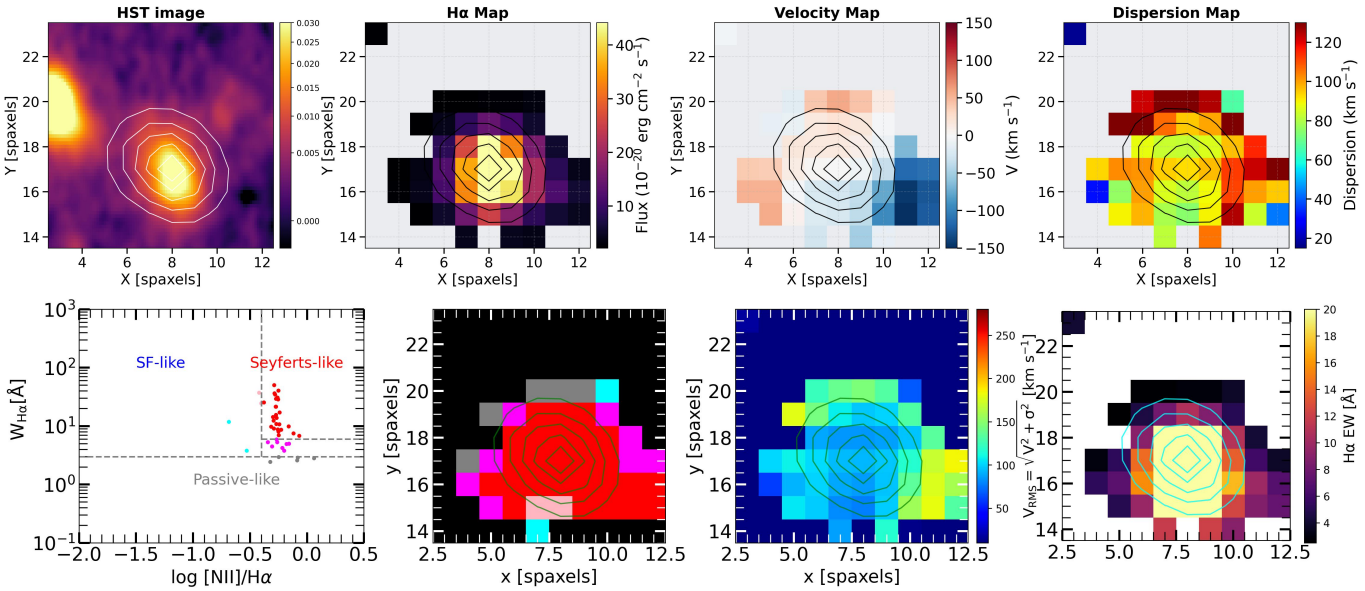


Figure 11. Spatially resolved maps for galaxy 6848. The panel layout and diagnostics shown are identical to those in Figure 8. The ionized gas is compact and dominated by nonstellar excitation. >95% of spaxels fall in the Seyfert regime of the WHAN diagram, with centrally concentrated high-excitation emission. The gas kinematics are moderately turbulent (typical $\sigma \gtrsim 100$ kms^{-1}) in the core, consistent with a compact AGN-photoionized region, with a possible signature of a nuclear outflow.

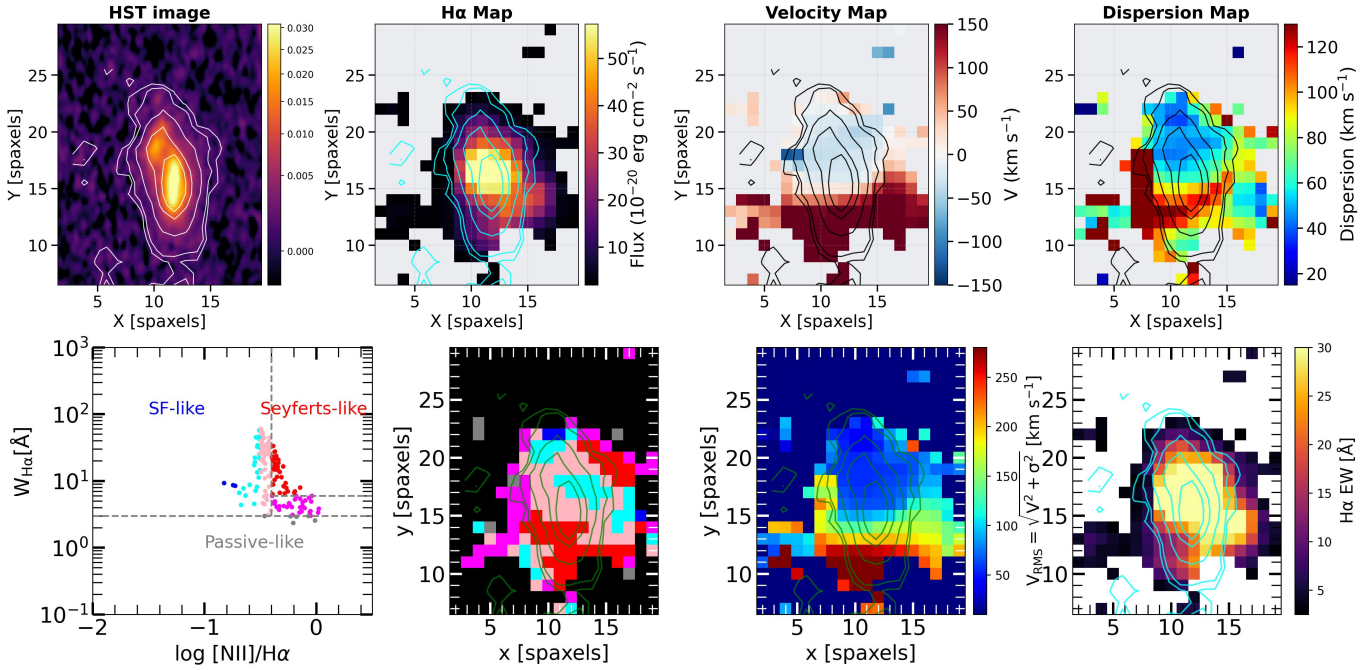


Figure 12. Spatially resolved maps for galaxy 13416. Resolved WHAN/BPT diagnostics reveal an inverted ionization pattern with off-nuclear Seyfert/LI(N)ER spaxels encircling a more SF-like center. The gas velocity field exhibits highly asymmetric values, reaching $v > 300$ km s^{-1} in the redshifted side, along with elevated σ. The kinematic values are consistent with a fast, off-nuclear outflow driving shock-excited emission.

pink, magenta, or red), implying that a substantial fraction of the ionized gas is excited by sources other than young, massive stars. Notably, the spaxels classified as "Seyfert-like" (red) are offset from the photometric center. Likewise, the magenta spaxels associated with shocks or LI(N)ER-like emission are off-nuclear and trace an outer annular structure. In contrast, spaxels classified as purely star-forming or transitional (cyan/pink) dominate the central region. This inverted ionization pattern—harder excitation at larger radii—suggests an extended, off-nuclear outflow, plausibly driven by SF or an AGN.

The ionized-gas kinematics reinforce this picture. The velocity field is highly asymmetric, with the redshifted side reaching $v = +316$ km s^{-1}, which is the largest amplitude in our sample and nearly 3 times that of the blueshifted side. These regions exhibit the highest velocity values across the

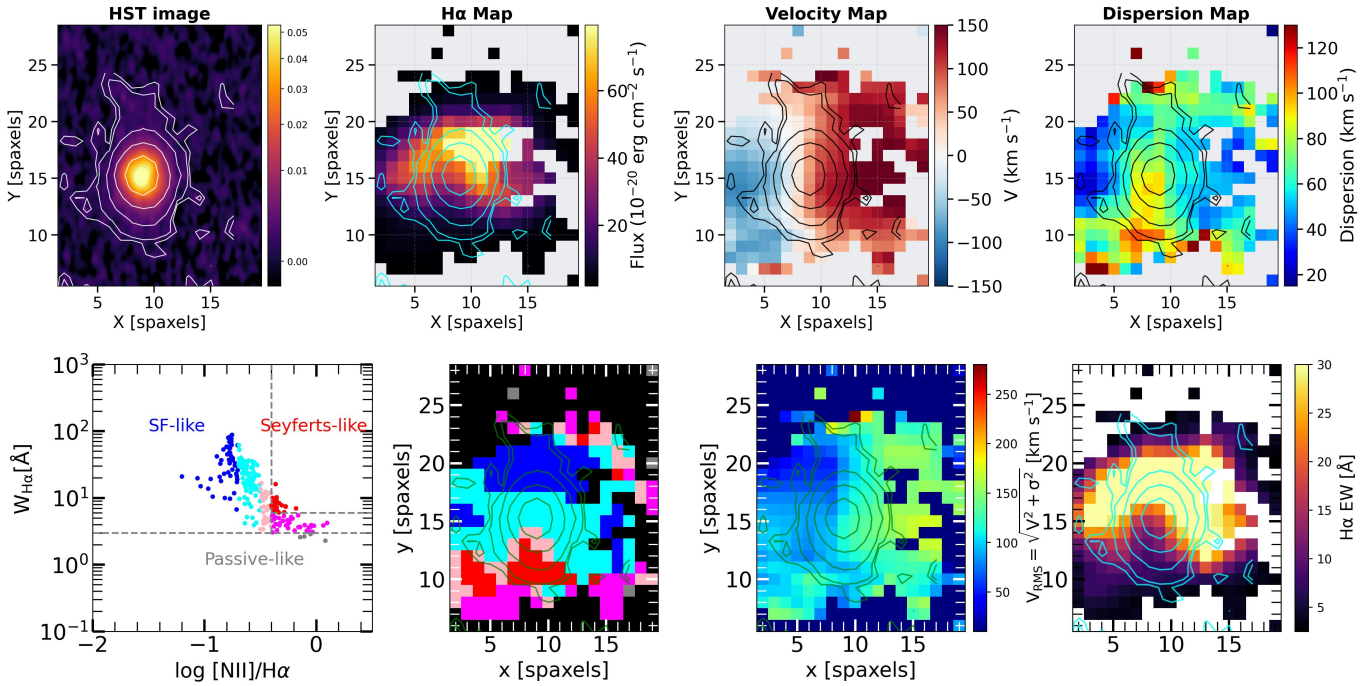


Figure 13. Resolved maps for galaxy 12015. The gas shows a rotating, disklike velocity gradient but is kinematically misaligned with the stellar major axis (gas is aligned E–W versus stellar photometric axis, which is N–S), with off-nuclear spaxels exhibiting Seyfert/LI(N)ER-like excitation along the outer edges, similar to Figure 12.

whole sample—almost 3 times larger in amplitude than even the blueshifted part of the galaxy. The velocity-dispersion map is similarly irregular and clumpy. The eastern side exhibits particularly elevated σ, where the shock-like/AGN-like ionization is observed. Line profiles display asymmetric wings (Figure 10), further supporting an outflow-driven shock interpretation.

The combination of high bulk velocities and broad dispersions is most naturally explained by fast, outflowing gas rather than by the inflow of newly accreted material. Such outflows could be powered by stellar feedback (e.g., supernovae or clustered stellar winds), consistent with the off-nuclear shock-excited spaxels. An alternative (and not mutually exclusive) scenario is a low-luminosity or obscured AGN. While no luminous central AGN is resolved in our MSA-3D data, a compact nucleus could evade detection at our spatial resolution (∼0.8 kpc at our redshift range) yet still drive galaxy-scale outflows that perturb the surrounding ISM (N. Roy et al. 2026).

Figure 13 shows that galaxy 12015 hosts a gas velocity gradient broadly consistent with disklike rotation oriented E–W, yet the gaseous kinematic axis is markedly misaligned with the stellar (photometric and stellar-kinematic) major axis, which is oriented N–S. Such a gas–star kinematic misalignment is a classic signature of nonequilibrium processes and points to either inflow or outflow superposed on the underlying rotation. Nebular line ratios further reveal mixed-ionization conditions: while most spaxels lie in the star-forming locus, there are notable off-nuclear regions with Seyfert/LI(N)ER-like excitation—similar to galaxy 13416, whose incidence increases toward larger radii (red/magenta/pink loci in the WHAN diagram), indicating a contribution from nonstellar ionizing sources.

Kinematically, the system is only moderately turbulent compared to the most disturbed AGN hosts in our sample: the mean dispersion is $\sigma_{\rm mean} = 76 \pm 10\,{\rm km\,s^{-1}}$, which is moderately higher than the dispersions found in typical star-forming disks at $z \sim 1$. The velocity field is relatively symmetric, and the second velocity moment remains modest with $V_{\rm rms}$, avg $\approx 115\,{\rm km\,s^{-1}}$, arguing against strong, galaxy-wide nongravitational motions. The off-nuclear Seyfert/LI(N)ER-like spaxels along the outer edges are indicative of features commonly seen in nearby IFU surveys (e.g., CALIFA, MaNGA), where low-ionization emission can arise from extended shocks (F. Belfiore et al. 2016; N. Roy et al. 2021a), photoionization by post-AGB populations (R. Yan & M. R. Blanton 2012), or diffuse/LLAGN illumination (J. J. Davies et al. 2024). In this context, galaxy 12015 appears to be predominantly SF dominated, but with localized, nonstellar ionization likely powered by boundary-layer shocks from supernovae-driven feedback and/or very weak AGN activity at the interfaces of turbulent structures.

3.6.4. IDs: 11843 and 8576—Galaxies with Tentative Signatures of Outflow

Galaxies 11843 and 8576 are similar because both galaxies show tentative signatures of ionized-gas flows superimposed on otherwise SF-dominated conditions. Spatially resolved diagnostics, shown in Figure 14, reveal that only a handful of spaxels have S/N > 3) in [N II] and display Seyfert- or LI(N)ER-like ratios, predominantly toward the outskirts. This suggests metal-poor ionized gas, primarily excited by evolved, LINER-like stellar populations (e.g., post-AGB). These non-star-forming spaxels are not randomly distributed. They coincide with localized pockets of enhanced turbulence traced by high σ from Hα line emission, with velocity dispersions $\sigma > 140\,{\rm km\,s^{-1}}$ and second velocity moments $V_{\rm rms} \gtrsim 300\,{\rm km\,s^{-1}}$. Elevated σ extends over a substantial N–S direction of the galaxy. Such extreme kinematics indicate

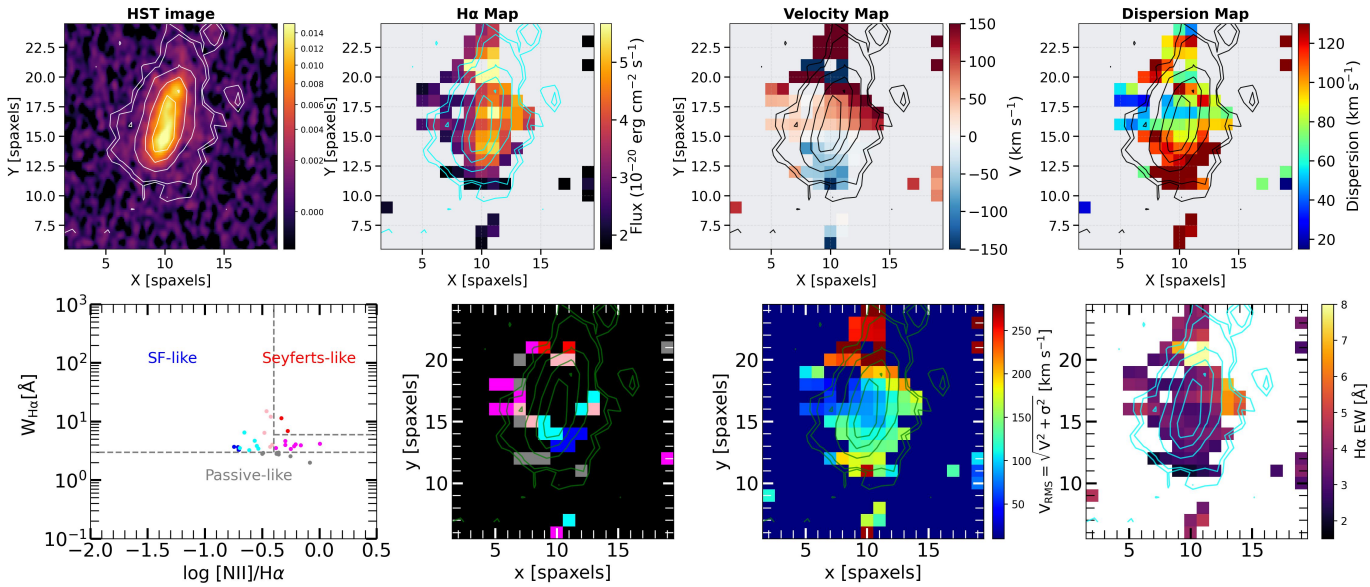


Figure 14. Maps for galaxy 11843. The panel layout and diagnostics shown are identical to those in Figure 8.

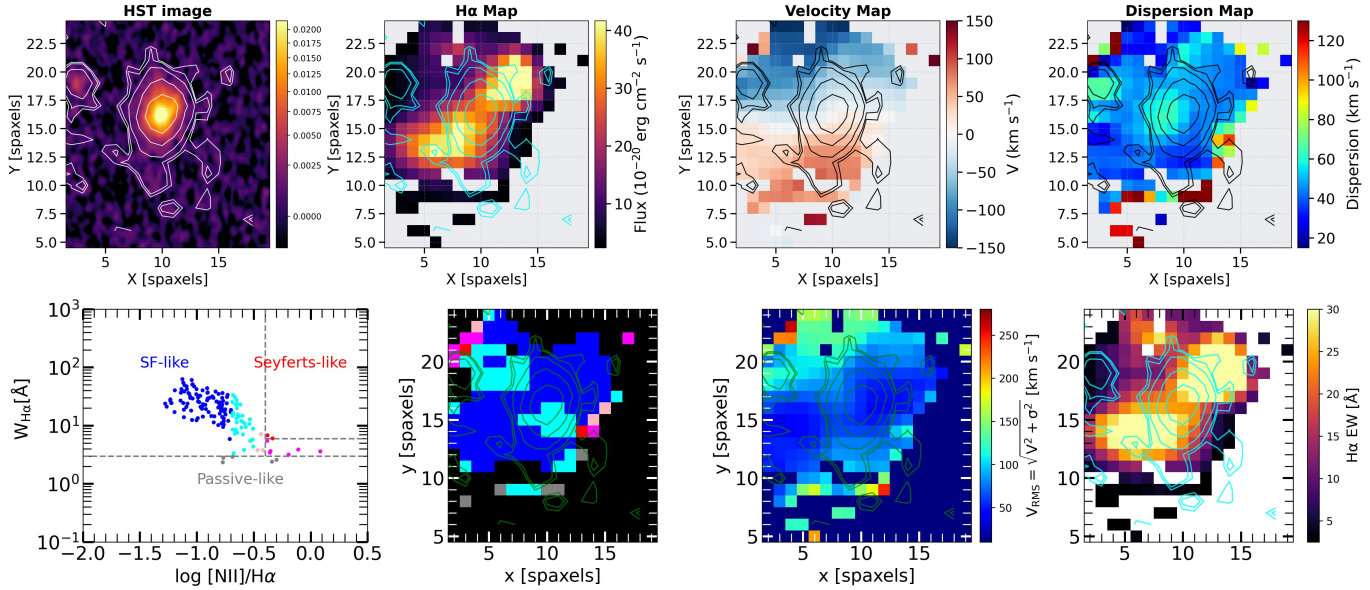


Figure 15. Maps for galaxy 8576. The panel layout and diagnostics shown are identical to those in Figure 8.

fast outflows or shock-heated gas. However, their scarcity across the footprint implies that any outflow present is compact and/or faint and insufficient to produce widespread shock-excited emission—and that much of the line emission may instead reflect low-equivalent width, LINER-like excitation. Consistently, the Hα equivalent-width map shows relatively low values across the galaxy.

In summary, the high-velocity, broad-line patches hint at outflow activity in galaxy 11843, but the limited spatial prevalence of nonstellar excitation suggests feedback that is weak, embedded, or operating below our current sensitivity. Deeper IFU observations will be required to determine the nature and scale of feedback in this intermediate system.

Galaxy 8576 likewise exhibits tentative evidence for gas flows atop a predominantly star-forming disk. Although $\gtrsim$95% of spaxels are consistent with photoionization by young stars as shown in Figure 15, the gaseous velocity field is kinematically misaligned with both the photometric major axis (from the HST image) and the stellar-continuum kinematic axis. This deviation from the symmetry expected for a purely rotation-supported system is commonly interpreted as a signature of radial gas motions—either inflow toward the center (C. Duckworth et al. 2019; J.-W. Zhou et al. 2021) or outflow escaping the disk (C. López-Cobá et al. 2019; D. Wylezalek et al. 2020; N. Roy et al. 2021a). In this system, the absolute kinematics are modest: $\sigma \lesssim 80\,\mathrm{km\,s^{-1}}$, and the second velocity moment peaks at $V_{\rm rms} \lesssim 125\,\mathrm{km\,s^{-1}}$. The H$\alpha$ equivalent width map shows elevated EW values ($\gtrsim$30 Å) in multiple clumps near the central region, consistent with concentrated SF, possibly driving supernovae-driven winds rather than AGN-driven feedback.

Galaxies 11843 and 8576 together occupy a transitional regime between orderly, rotation-dominated disks and systems with a clear signature of outflows. They may represent early

stages of feedback or environmental influence where the dynamical impact on the ISM precedes any substantial ionization shift. As emphasized by recent work (R. L. Davies et al. 2019; D. Wylezalek et al. 2022), disentangling such subtle transitions requires spatially resolved kinematics and detailed ionization diagnostics to uncover the origin of disturbed gas in otherwise normal-looking galaxies.

4. Discussion

The six AGN/outflow candidates identified here illustrate the power of spatially resolved spectroscopy to uncover weak or obscured nuclear activity that is invisible in integrated light. Although their global line ratios would classify them as ordinary star-forming galaxies, the resolved maps reveal compact zones of enhanced excitation, elevated velocity dispersion, and—in some cases—broad emission-line components (Figure 10) indicative of nonstellar ionization. A key feature of these candidates is the presence of compact regions that exhibit subsets of spaxels crossing the L. J. Kewley et al. (2001) theoretical boundary for pure SF on the BPT diagram or fall to the AGN/LINER-like region of the WHAN diagnostic (R. Cid Fernandes et al. 2011). This points to contributions from LLAGN-driven photoionization, outflows, and/or shock-heated gas. Similar phenomena have been reported in nearby $z < 0.1$ galaxies, where spatially resolved IFU surveys (R. Davies et al. 2020; N. Roy et al. 2021a; G. Venturi et al. 2021) have revealed AGN-like excitation in galaxies that are otherwise classified as purely star-forming or quenched. In what follows, we estimate key ISM properties, approximate AGN luminosities for these candidates, and derive characteristic mass-loss rates associated with their warm-ionized outflows.

4.1. Ionization and Density: Inferences from Line Ratio Gradients of Galaxies with Outflows, Shocks, and AGNs

In this section, we will characterize the physical conditions like ionized-gas-density and ionization properties in these candidate systems. We will then utilize these measurements to constrain the properties of the associated outflows. Electron density (n_e) in these sources is derived from the [S II] $\lambda\lambda$6717, 6731 doublet ratio, which is sensitive to the density of the ionized gas. This diagnostic is only available for a subset of MSA-3D galaxies where the redshifted [S II] doublet falls within the NIRSpec G140H/F100LP wavelength range (I. Barišić et al. 2025). We fit the line profiles with a two-component Gaussian model and compute the flux ratio, converting it to electron density under the assumption of $T_e = 10^4$ K (D. E. Osterbrock & G. J. Ferland 2006). The resulting n_e values in the galaxies hosting AGN/outflow signatures range from 50 to 200 cm^{-3}, consistent with typical conditions in ionized outflows (L. J. Kewley et al. 2019; R. Davies et al. 2020). For comparison, the median [SII] ratio across the full MSA-3D sample is ∼1.39, which is consistent with the mean ratio of 1.38 observed in star-forming galaxies at $z \sim 0$ from MaNGA (F. Belfiore et al. 2016), corresponding to $n_e \sim 30$ cm^{-3}. Our AGN candidates thus span a broader and generally higher range in electron density compared to typical star-forming galaxies.

While powerful AGNs are capable of photoionizing gas over large distances, their lower-luminosity counterparts may not provide sufficient ionizing photons to explain the observed emission-line luminosities. For LLAGNs, it is crucial to determine whether the AGN alone can account for the observed nebular excitation. Typical star-forming galaxies at $z \sim 1$–1.5 are inferred to have ionization parameters of an order $\log U \sim -2.8$ to -2.3 from previous studies (M. Kaasinen et al. 2018; R. L. Sanders et al. 2020), with representative main-sequence systems lying near $\log U \approx -2.8$ and higher-excitation auroral-line samples reaching median values of $\log U \approx -2.3$. We therefore adopt the midpoint of this range, $\log U = -2.5$, which is also broadly consistent with the values inferred for the four MSA-3D galaxies for which both [O III]λ5007 and [O II] λ3727 are available. Using this ionization parameter along with the mean measured electron density of $n_e \sim 110$ cm^{-3} for our AGN sample and a radial extent of $r \sim 5$ kpc (based on the approximate spatial distribution of the ionized gas), we estimate the required ionizing photon rate to be $Q \approx 3 \times 10^{55}$ photons s^{-1}. To relate this to AGN bolometric luminosity, we adopt the average SED of quasars from M. Elvis et al. (1994), where the extreme-UV slope follows $f_\nu \propto \nu^{-1.8}$. This yields a conversion of $L_{\rm AGN}/Q \approx (2-6) \times 10^{-11}$ erg, implying that the AGN would require a bolometric luminosity of $L_{\rm AGN} \approx 1.2 \times 10^{45}$ erg s^{-1} to sustain the observed ionization level over 5 kpc.

However, this required $L_{\rm AGN}$ exceeds the AGN luminosities derived from [O III] λ5007 or Hα emission in the center of our sources by at least an order of magnitude. Thus, the central AGNs alone cannot supply enough ionizing photons to explain the full extent of the observed nebulae. This suggests that additional ionization sources must be contributing—such as young massive stars, shocks, or evolved stellar populations. This interpretation is further supported by resolved line ratio diagnostics, which indicate that 20%–40% of the spaxels in these galaxies lie in BPT/WHAN regions consistent with SF. Hence, young stellar populations likely provide a substantial fraction of the ionizing radiation.

Shocks may also play an important role. Previous work has shown that AGNs exhibiting shock-dominated ionization often display large velocity widths in forbidden lines such as [O III] and [O II] (N. Roy et al. 2021a). Although the maximum observed FWHMs in our sample ($\lesssim$300 km s^{-1}) are somewhat lower than in classical shock-dominated systems, contribution of shocks can still be nonnegligible. In summary, these findings suggest that the observed nebular ionization arises from a composite of photoionization by weak AGNs, ongoing SF, and possibly radiative shocks driven by outflows—each of which plays a varying role across spatial scales.

4.2. Outflow Rates and Energetics for AGN Candidates

In this section, we estimate key physical quantities characterizing warm-ionized outflows in the six AGN/outflow candidates identified in the previous section. We quantify the total ionized-gas mass, mass outflow rate, kinetic power, and momentum flux, focusing on the warm $\sim 10^4$ K gas phase of the ISM. We use the electron density n_e measurement from Section 4.1 using the [S II] $\lambda\lambda$6717, 6731 doublet. The ionized-gas mass associated with the outflow is calculated following the prescription of G. Cresci et al. (2023):

$$M_{\rm out} = 3.2 \times 10^5 \quad \frac{L_{\rm out},\, {\rm H}\alpha}{10^{40}\ {\rm erg\ s^{-1}}} \frac{100\ {\rm cm^{-3}}}{n_{\rm e},\, {\rm out}} \quad M_\odot \qquad (1)$$

where $L_{\rm out}$, Hα is the Hα luminosity associated with the outflowing gas, and n_e is the measured electron density. The

Hα luminosity used here is measured from the set of spaxels that satisfy our outflow-candidate criteria, i.e., regions with disturbed kinematics and non-star-forming line ratios. We use the total Hα flux within these outflow regions, instead of performing a spaxel-by-spaxel separation of narrow and broad components, since the majority of our sample do not show multikinematic components in the resolved emission-line profiles. For the three galaxies that do show clear two-component kinematic structure, the outflow quantities derived from the broad-component fits differ by ∼20% from those based on the single-component measurements over the same disturbed regions. We thus adopt the single-component measurements for consistency across the full candidate sample. The typical Hα luminosity associated with outflow spaxels ranges within $\sim 2 \times 10^{41} - 3 \times 10^{42}$ erg s^{-1} for our six galaxies. Applying this to our sources, we find ionized-gas masses ranging from 3×10^6 to $4 \times 10^7\, M_\odot$.

Once the outflow mass is derived, the mass outflow rate for the outflowing gas can be derived by

$$\dot{M}_{\rm out} = \frac{M_{\rm out}\, v_{\rm out}}{\Delta R_{\rm out}}. \quad (2)$$

Here, $\Delta R_{\rm out}$ represents the deprojected radial distance of the outflowing gas parcels from the host galaxy center, defined by the peak of the stellar-continuum map. For our sample, the total projected extent of the outflowing gas spans ∼5−8 kpc, so we adopt $\Delta R_{\rm out} \sim 3$ kpc, corresponding to the median radial extent. The outflow velocity is estimated as $v_{\rm out} = \sqrt{\sigma^2 + \Delta v^2}$, where σ is the velocity dispersion of the outflowing component, and Δv is the velocity shift relative to systemic. Using this method, we find $\dot{M}_{\rm out} \sim 1 - 4\, M_\odot$ yr^{-1} across the sample.

The corresponding kinetic power of the outflow is given by

$$\dot{\rm KE}_{\rm outflow} = \frac{1}{2} \times \dot{M}_{\rm out}\, v_{\rm out}^2. \quad (3)$$

The resultant kinetic power (or the kinetic energy injection rates) lies between 0.7 and 1.3×10^{41} erg s^{-1}. Various feedback models and simulations suggest that, for AGNs to drive energetically powerful winds to inject adequate energy into the ISM, the kinetic power of the outflow must be 0.5%–5% of the AGN bolometric luminosity ($L_{\rm AGN}$) (T. Di Matteo et al. 2005; P. F. Hopkins & M. Elvis 2010). To assess this, we estimate an upper limit on $L_{\rm AGN}$ from central [O III] or Hα luminosities measured within a 0.″1 aperture, using empirical scaling relations (T. M. Heckman & P. N. Best 2014). Our $L_{\rm AGN}$ ranges from 10^{43} to 10^{44} erg s^{-1}, which implies kinetic coupling efficiencies of ∼0.1%−1%. This places our sources within the theoretically expected regime where AGN-driven outflows can meaningfully impact the surrounding ISM, despite their modest luminosities.

To contextualize our results, Figure 16 compares the derived $\dot{M}_{\rm out}$ and L_{AGN} for our MSA-3D AGN/outflow sources to literature AGN-driven outflow measurements spanning a broad redshift range ($z \sim 0.05-6$). The comparison sample includes nearby low-z quasars (circles, N. P. H. Nesvadba et al. 2006; M. Brusa et al. 2016; M. Revalski et al. 2018; T. T. Shimizu et al. 2019; D. Kakkad et al. 2022), high-z ($z > 3.5$) radio galaxies (triangles, N. Roy et al. 2024, 2026; A. Saxena et al. 2024; W. Wang et al. 2024, 2025), and luminous unobscured

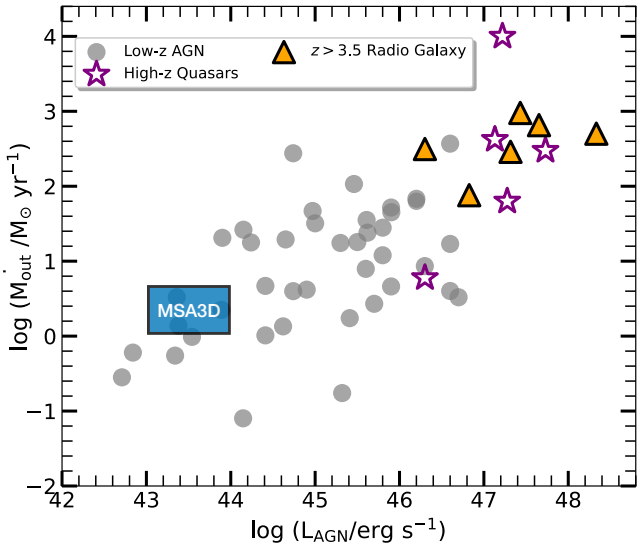


Figure 16. The integrated mass outflow rate versus AGN bolometric luminosity for AGN sources in the MSA-3D sample (blue box) compared to sources reported in the literature using a variety of IFU/long-slit spectroscopy. Gray symbols indicate low-redshift ($z < 0.1$) quasars (N. P. H. Nesvadba et al. 2006; M. Brusa et al. 2016; M. Revalski et al. 2018; B. Dall'Agnol de Oliveira et al. 2021; M. Revalski et al. 2021; D. Kakkad et al. 2022), the purple stars indicate JWST/IFU observations of radio-quiet quasars at high redshifts ($1 < z < 6$; G. Cresci et al. 2023; M. A. Marshall et al. 2023; S. Veilleux et al. 2023), and yellow triangles represent high-z ($z > 3.5$) radio galaxies (N. Roy et al. 2024; W. Wang et al. 2024, 2025; N. Roy et al. 2026). We find that the MSA-3D sources align with the broader trend between $\dot{M}_{\rm out}$ and $L_{\rm AGN}$, overlapping the low-luminosity distribution of AGN at $z \sim 0.1$. Their mass outflow rates constitute the lowest tail of the distribution of $z \sim 0$ AGNs.

quasars with spatially resolved outflows (stars, G. Cresci et al. 2023; M. Perna et al. 2023; A. Vayner et al. 2024; S. Veilleux et al. 2023). Importantly, we restrict the sample to studies using directly measured n_e and $v_{\rm out}$ from spatially resolved IFU observations to ensure consistency in the derived energetics.

We find that the MSA-3D sources align with the broader trend between $\dot{M}_{\rm out}$ and $L_{\rm AGN}$, despite being powered by LLAGNs. Their mass outflow rates constitute the lowest tail of the distribution for the detected AGNs and quasars, suggesting that even some of the lowest-luminosity AGN activity at $z \sim 1$ can drive modest outflows, and may have a similar effect as the powerful AGNs in the local Universe. This highlights the key role of LLAGNs especially at higher redshifts, and emphasizes the importance of identifying this elusive population through spatially resolved spectroscopic diagnostics.

4.3. Detection Limits and Completeness of Resolved AGN/Outflow Signatures in MSA-3D

In the previous sections, we demonstrated that spatially resolved spectroscopy from the MSA-3D survey allows us to uncover weak AGN activity, shocks, or disturbed ionized-gas signatures, which are mostly invisible in integrated spectra. Our selection is not based on any single diagnostic alone. We identify candidate systems when they host at least three contiguous spaxels where BPT/WHAN line ratios suggest nonstellar or mixed excitation and when those same regions also show disturbed ionized-gas kinematics. These kinematic signatures include elevated σ or $V_{\rm rms}$, misalignment between the ionized-gas and stellar-kinematic axes, or asymmetric and multicomponent line profiles where the S/N is sufficient.

It is important to emphasize that we do not use $V_{\rm rms}$ as a stand-alone outflow threshold. The quantity $V_{\rm rms} = \sqrt{v^2 + \sigma^2}$ includes both ordered velocity gradients and local line broadening. Therefore, in massive or inclined rotating disks, and especially near galaxy centers where beam smearing can be important, high $V_{\rm rms}$ values may not necessarily indicate outflowing gas. In this work, we use elevated $V_{\rm rms}$ only as a tracer for kinematically disturbed regions. We then check whether those regions are spatially coherent, whether they coincide with enhanced or mixed line ratios, and if the morphology or line profiles support a noncircular gas motion interpretation. This conservative selection naturally introduces incompleteness. Compact AGN narrow-line regions, weak shocks, or slow outflows that do not form coherent multispaxel structures may easily escape detection. Similarly, systems whose line ratios remain compatible with H II-region excitation, or whose disturbed kinematics fall below our sensitivity, may only be classified as tentative or mixed-ionization cases. Thus, our sample likely represents the more detectable end of weak AGN, shock, and outflow signatures in the current MSA-3D data.

The sensitivity of the MSA-3D observations further sets a practical limit on the faintest AGN that can be detected with MSA-3D. From the measured emission-line and continuum levels, the 5σ line-detection threshold corresponds to an [O III] λ5007 flux of $\sim 2 \times 10^{-19}$ erg cm^{-2} s^{-1}. For the distances of our targets and standard [O III]-to-bolometric conversions, this flux limit implies a characteristic AGN bolometric luminosity of $L_{\rm AGN} \approx 10^{43}$erg s^{-1}. Sources with intrinsically fainter AGN or additional continuum dilution would therefore fall below our detection sensitivity. This imposes a conservative luminosity floor of $L_{\rm AGN} \gtrsim 10^{43}$ erg s^{-1} for AGNs detected through spatially resolved line emission in the MSA-3D data. Similarly, slow or compact outflows that do not extend over multiple spaxels or reach high-velocity dispersion may also go undetected, even if physically present. Despite these limitations, this represents a significant improvement over traditional integrated-light spectroscopy. We identify six candidates, but only two would have been identified as non-star-forming from traditional BPT/WHAN diagnostics from integrated spectra. Expanding MSA-3D-type surveys to deeper sensitivities, finer spatial resolution, and broader wavelength coverage will be the key to uncovering the full population of faint AGNs and low-level feedback at cosmic noon.

5. Conclusions

We present spatially resolved rest-optical spectroscopy for 38 star-forming galaxies at ($0.5 < z < 1.5$) from the JWST/NIRSpec MSA-3D survey, which uses slit-stepping to build IFU-like data cubes at $0\farcs1$ spatial sampling. With maps of [N II]/Hα, [S II]/Hα, [O III]/Hβ, and [N II]/[S II], we compare internal excitation and kinematics and place them in context with $z \sim 0$ IFU results. At fixed stellar mass relative to local galaxies, our $z \sim 1$ galaxies show systematically lower [N II]/Hα and [S II]/Hα and higher [O III]/Hβ, consistent with lower metallicities and harder radiation fields. Radially, [N II]/Hα is typically flat or mildly negative, [S II]/Hα rises with radius, [O III]/Hβ is flat or slightly positive, and [N II]/[S II] declines with radius. These trends imply only weak radial variation in O/H but a systematic change in ionization structure: the rise in [S II]/Hα points to an increasing contribution from DIG and/or a lower ionization parameter at larger radii, while the positive [O III]/Hβ is consistent with mildly declining metallicity and harder radiation fields in the outskirts. The declining [N II]/[S II] further indicates an outward decrease in N/O, as expected for inside-out chemical enrichment with delayed secondary nitrogen production.

A key result is a positive correlation between [N II]/Hα and the velocity dispersion σ in kiloparsec-scale, linking local excitation sources to turbulent kinematics. While integrated BPT/WHAN diagnostics largely place the galaxies in the star-forming regime, resolved maps reveal compact zones with AGN/Seyfert- or LINER-like excitation and elevated σ. Six galaxies, i.e., $\sim$16% of the sample, host coherent, non-star-forming ionized regions with enhanced [N II]/Hα, high $V_{\rm rms} = \sqrt{v^2 + \sigma^2}$, and in some cases broad components, indicating weak AGN activity and/or outflows.

For these candidates, inferred warm-ionized outflow rates are modest ($\sim 1-4\, M_\odot\, {\rm yr}^{-1}$) with kinetic powers $\sim$0.1%$-$1% of $L_{\rm AGN}$, placing them at the low-energy tail of known AGN-driven winds yet on the same global $\dot{M}_{\rm out}$–$L_{\rm AGN}$ trend. The survey sensitivity implies completeness for detecting AGN activity with $L_{\rm AGN} \gtrsim 10^{43}$ erg s^{-1} and outflows $\gtrsim$2 kpc^2 in size, highlighting both the potential and current limitations of detecting faint feedback at $z \sim 1$ using spatially resolved spectroscopy.

Acknowledgments

This work is based on observations made with the NASA/ESA/CSA James Webb Space Telescope. The data were obtained from the Mikulski Archive for Space Telescopes (MAST) at the Space Telescope Science Institute, which is operated by the Association of Universities for Research in Astronomy, Inc., under NASA contract NAS 5-03127. These observations are associated with program PID 2136. The data processing was performed using the JWST Science Calibration Pipeline and the JWST Calibration Reference Data System (CRDS). The JWST data presented in this article can be accessed from MAST via doi:10.17909/8hkf-4e47. N.R. acknowledges support from the School of Earth and Space Exploration (SESE) through the Exploration Fellowship. We acknowledge financial support from NASA through grant JWST-GO-2136. This work made use of observations and catalogs from the 3DHST Treasury Program (GO 12177 and 12328) with the NASA/ ESA Hubble Space Telescope, which is operated by the Association of Universities for Research in Astronomy, Inc., under NASA contract NAS5-26555.

ORCID iDs

Namrata Roy https://orcid.org/0000-0002-4430-8846
Alaina Henry https://orcid.org/0000-0002-6586-4446
Tucker Jones https://orcid.org/0000-0001-5860-3419
Ivana Barišić https://orcid.org/0000-0001-6371-6274
Ryan L. Sanders https://orcid.org/0000-0003-4792-9119
Kevin Bundy https://orcid.org/0000-0001-9742-3138
Matthew A. Malkan https://orcid.org/0000-0001-6919-1237
Themiya Nanayakkara https://orcid.org/0000-0003-2804-0648
Karl Glazebrook https://orcid.org/0000-0002-3254-9044
Timothy Heckman https://orcid.org/0000-0001-6670-6370
Juan M. Espejo Salcedo https://orcid.org/0000-0001-6703-4676
Xin Wang https://orcid.org/0000-0002-9373-3865
Danail Obreschkow https://orcid.org/0000-0002-1527-0762
Tommaso Treu https://orcid.org/0000-0002-8460-0390

References

Backhaus, B. E., Trump, J. R., Pirzkal, N., et al. 2024, ApJ, 962, 195
Baldwin, J. A., Phillips, M. M., & Terlevich, R. 1981, PASP, 93, 5
Barišić, I., Jones, T., Mortensen, K., et al. 2025, ApJ, 983, 139
Belfiore, F., Maiolino, R., Maraston, C., et al. 2016, MNRAS, 461, 3111
Belfiore, F., Maiolino, R., Tremonti, C., et al. 2017, MNRAS, 469, 151
Berg, D. A., Pogge, R. W., Skillman, E. D., et al. 2020, ApJ, 893, 96
Brusa, M., Perna, M., Cresci, G., et al. 2016, A&A, 588, A58
Bundy, K., Bershady, M. A., Law, D. R., et al. 2015, ApJ, 798, 7
Cameron, A. J., Saxena, A., Bunker, A. J., et al. 2023, A&A, 677, A115
Cappellari, M., Bacon, R., Bureau, M., et al. 2006, MNRAS, 366, 1126
Cheung, E., Bundy, K., Cappellari, M., et al. 2016, Natur, 533, 504
Cid Fernandes, R., Stasińska, G., Mateus, A., & Vale Asari, N. 2011, MNRAS, 413, 1687
Claeyssens, A., Adamo, A., Richard, J., et al. 2023, MNRAS, 520, 2180
Coil, A. L., Aird, J., Reddy, N., et al. 2015, ApJ, 801, 35
Cresci, G., Mainieri, V., Brusa, M., et al. 2015, ApJ, 799, 82
Cresci, G., Tozzi, G., Perna, M., et al. 2023, A&A, 672, A128
Curti, M., D'Eugenio, F., Carniani, S., et al. 2023, MNRAS, 518, 425
D'Agostino, J. J., Kewley, L. J., Groves, B. A., et al. 2019, MNRAS, 487, 4153
Dall'Agnol de Oliveira, B., Storchi-Bergmann, T., Kraemer, S. B., et al. 2021, MNRAS, 504, 3890
Davies, J. J., Pontzen, A., & Crain, R. A. 2024, MNRAS, 527, 4705
Davies, R., Baron, D., Shimizu, T., et al. 2020, MNRAS, 498, 4150
Davies, R. L., Förster Schreiber, N. M., Übler, H., et al. 2019, ApJ, 873, 122
Di Matteo, T., Springel, V., & Hernquist, L. 2005, Natur, 433, 604
Duckworth, C., Tojeiro, R., Kraljic, K., et al. 2019, MNRAS, 483, 172
Elmegreen, B. G. 2007, ApJ, 668, 1064
Elvis, M., Wilkes, B. J., McDowell, J. C., et al. 1994, ApJS, 95, 1
Emsellem, E., Schinnerer, E., Santoro, F., et al. 2022, A&A, 659, A191
Finkelstein, S. L., Leung, G. C. K., Bagley, M. B., et al. 2024, ApJL, 969, L2
Förster Schreiber, N. M., Genzel, R., Newman, S. F., et al. 2014, ApJ, 787, 38
Förster Schreiber, N. M., Übler, H., Davies, R. L., et al. 2019, ApJ, 875, 21
Genzel, R., Newman, S., Jones, T., et al. 2011, ApJ, 733, 101
Glazebrook, K. 2013, PASA, 30, e056
Harikane, Y., Zhang, Y., Nakajima, K., et al. 2023, ApJ, 959, 39
Heckman, T. M., & Best, P. N. 2014, ARA&A, 52, 589
Hemler, Z. S., Torrey, P., Qi, J., et al. 2021, MNRAS, 506, 3024
Henry, A., Rafelski, M., Sunnquist, B., et al. 2021, ApJ, 919, 143
Hopkins, P. F., & Elvis, M. 2010, MNRAS, 401, 7
Ju, M., Wang, X., Jones, T., et al. 2025, ApJL, 978, L39
Kaasinen, M., Kewley, L., Bian, F., et al. 2018, MNRAS, 477, 5568
Kakkad, D., Sani, E., Rojas, A. F., et al. 2022, MNRAS, 511, 2105
Kashino, D., Silverman, J. D., Sanders, D., et al. 2017, ApJ, 835, 88
Kauffmann, G., Heckman, T. M., Tremonti, C., et al. 2003, MNRAS, 346, 1055
Kewley, L. J., & Dopita, M. A. 2002, ApJS, 142, 35
Kewley, L. J., Dopita, M. A., Sutherland, R. S., Heisler, C. A., & Trevena, J. 2001, ApJ, 556, 121
Kewley, L. J., Groves, B., Kauffmann, G., & Heckman, T. 2006, MNRAS, 372, 961
Kewley, L. J., Nicholls, D. C., & Sutherland, R. S. 2019, ARA&A, 57, 511
Kocevski, D. D., Finkelstein, S. L., Barro, G., et al. 2025, ApJ, 986, 126
Koekemoer, A. M., Faber, S. M., Ferguson, H. C., et al. 2011, ApJS, 197, 36
Kokorev, V., Chisholm, J., Endsley, R., et al. 2024, ApJ, 975, 178
Kriek, M., Shapley, A. E., Reddy, N. A., et al. 2015, ApJS, 218, 15
Labbé, I., van Dokkum, P., Nelson, E., et al. 2023, Natur, 616, 266
Lacerda, E. A. D., Cid Fernandes, R., Couto, G. S., et al. 2018, MNRAS, 474, 3727
López-Cobá, C., Sánchez, S. F., Bland-Hawthorn, J., et al. 2019, MNRAS, 482, 4032
Ma, X., Hopkins, P. F., Feldmann, R., et al. 2017, MNRAS, 466, 4780
Maiolino, R., & Mannucci, F. 2019, A&ARv, 27, 3
Maiolino, R., Scholtz, J., Curtis-Lake, E., et al. 2024, A&A, 691, A145
Mannucci, F., Cresci, G., Maiolino, R., Marconi, A., & Gnerucci, A. 2010, MNRAS, 408, 2115
Mármol-Queraltó, E., McLure, R. J., Cullen, F., et al. 2016, MNRAS, 460, 3587
Marshall, M. A., Perna, M., Willott, C. J., et al. 2023, A&A, 678, A191
Masters, D., Faisst, A., & Capak, P. 2016, ApJ, 828, 18
Matthee, J., Naidu, R. P., Brammer, G., et al. 2024, ApJ, 963, 129
Momcheva, I. G., Brammer, G. B., van Dokkum, P. G., et al. 2016, ApJS, 225, 27
Nakajima, K., Ouchi, M., Isobe, Y., et al. 2023, ApJS, 269, 33
Nesvadba, N. P. H., Lehnert, M. D., Eisenhauer, F., et al. 2006, ApJ, 650, 693
Newman, J. A., Cooper, M. C., Davis, M., et al. 2013, ApJS, 208, 5
Osterbrock, D. E., & Ferland, G. J. 2006, in Astrophysics of Gaseous Nebulae and Active Galactic Nuclei, ed. D. E. Osterbrock & G. J. Ferland (Univ. Science Books)
Perna, M., Arribas, S., Marshall, M., et al. 2023, A&A, 679, A89
Pettini, M., & Pagel, B. E. J. 2004, MNRAS, 348, L59
Revalski, M., Crenshaw, D. M., Kraemer, S. B., et al. 2018, ApJ, 856, 46
Revalski, M., Meena, B., Martinez, F., et al. 2021, ApJ, 910, 139
Riffel, R. A., Riffel, R., Storchi-Bergmann, T., et al. 2024, MNRAS, 528, 1476
Rosales-Ortega, F. F., Sánchez, S. F., Iglesias-Páramo, J., et al. 2012, ApJL, 756, L31
Roy, N., Heckman, T., & Henry, A. 2026, ApJ, 1002, 57
Roy, N., Bundy, K., Cheung, E., et al. 2018, ApJ, 869, 117
Roy, N., Bundy, K., Nevin, R., et al. 2021a, ApJ, 913, 33
Roy, N., Bundy, K., Rubin, K. H. R., et al. 2021b, ApJ, 919, 145
Roy, N., Moravec, E., Bundy, K., et al. 2021c, ApJ, 922, 230
Roy, N., Heckman, T., Overzier, R., et al. 2024, ApJ, 970, 69
Sánchez, A. G., Kazin, E. A., Beutler, F., et al. 2013, MNRAS, 433, 1202
Sánchez, S., Sánchez-Menguiano, L., Marino, R., et al. 2015, Galax, 3, 164
Sánchez, S. F., García-Benito, R., Zibetti, S., et al. 2016, A&A, 594, A36
Sanders, R. L., Shapley, A. E., Topping, M. W., Reddy, N. A., & Brammer, G. B. 2023, ApJ, 955, 54
Sanders, R. L., Shapley, A. E., Zhang, K., & Yan, R. 2017, ApJ, 850, 136
Sanders, R. L., Shapley, A. E., Jones, T., et al. 2021, ApJ, 914, 19
Sanders, R. L., Shapley, A. E., Kriek, M., et al. 2016, ApJ, 816, 23
Sanders, R. L., Shapley, A. E., Reddy, N. A., et al. 2020, MNRAS, 491, 1427
Sanders, R. L., Shapley, A. E., Topping, M. W., et al. 2026, ApJ, 1003, 228
Sarzi, M., Shields, J. C., Schawinski, K., et al. 2010, MNRAS, 402, 2187
Saxena, A., Overzier, R. A., Villar-Martín, M., et al. 2024, MNRAS, 531, 4391
Schawinski, K., Thomas, D., Sarzi, M., et al. 2007, MNRAS, 382, 1415
Shajib, A. J., Treu, T., Melo, A., et al. 2025, A&A, 702, L12
Shapley, A. E., Reddy, N. A., Kriek, M., et al. 2015, ApJ, 801, 88
Shapley, A. E., Sanders, R. L., Reddy, N. A., Topping, M. W., & Brammer, G. B. 2023, ApJ, 954, 157
Shapley, A. E., Sanders, R. L., Shao, P., et al. 2019, ApJL, 881, L35
Shapley, A. E., Sanders, R. L., Topping, M. W., et al. 2025, ApJ, 980, 242
Shimizu, T. T., Davies, R. I., Lutz, D., et al. 2019, MNRAS, 490, 5860
Shivaei, I., Reddy, N. A., Shapley, A. E., et al. 2015, ApJ, 815, 98
Stasińska, G., Cid Fernandes, R., Mateus, A., Sodré, L., & Asari, N. V. 2006, MNRAS, 371, 972
Stefanon, M., Labbé, I., Bouwens, R. J., et al. 2017, ApJ, 851, 43
Steidel, C. C., Rudie, G. C., Strom, A. L., et al. 2014, ApJ, 795, 165
Strom, A. L., Steidel, C. C., Rudie, G. C., et al. 2017, ApJ, 836, 164
Topping, M. W., Sanders, R. L., Shapley, A. E., et al. 2025, MNRAS, 541, 1707
Trump, J. R., Arrabal Haro, P., Simons, R. C., et al. 2023, ApJ, 945, 35
Übler, H., D'Eugenio, F., Perna, M., et al. 2024, MNRAS, 533, 4287
van der Wel, A., Franx, M., van Dokkum, P. G., et al. 2014, ApJ, 788, 28
Vayner, A., Zakamska, N. L., Ishikawa, Y., et al. 2024, ApJ, 960, 126
Veilleux, S., Liu, W., Vayner, A., et al. 2023, ApJ, 953, 56
Veilleux, S., & Osterbrock, D. E. 1987, ApJS, 63, 295
Venturi, G., Cresci, G., Marconi, A., et al. 2021, A&A, 648, A17
Wang, W., De Breuck, C., Wylezalek, D., et al. 2025, A&A, 696, A88
Wang, W., Wylezalek, D., De Breuck, C., et al. 2024, A&A, 683, A169
Whitaker, K. E., Franx, M., Leja, J., et al. 2014, ApJ, 795, 104
Wisnioski, E., Förster Schreiber, N. M., Fossati, M., et al. 2019, ApJ, 886, 124
Wisnioski, E., Förster Schreiber, N. M., Wuyts, S., et al. 2015, ApJ, 799, 209
Wylezalek, D., Flores, A. M., Zakamska, N. L., Greene, J. E., & Riffel, R. A. 2020, MNRAS, 492, 4680
Wylezalek, D., Zakamska, N. L., Greene, J. E., et al. 2018, MNRAS, 474, 1499
Wylezalek, D., Vayner, A., Rupke, D. S. N., et al. 2022, ApJL, 940, L7
Xia, J., Malkan, M. A., Ross, N. R., & Ancheta, A. J. 2018, ApJ, 869, 138
Yan, R., & Blanton, M. R. 2012, ApJ, 747, 61
Zhang, K., Yan, R., Bundy, K., et al. 2017, MNRAS, 466, 3217
Zhou, J.-W., Liu, T., Li, J.-Z., et al. 2021, MNRAS, 508, 4639